Plume-Lithosphere interaction and its effect on surface topography: A theoretical and experimental approach

Thesis submitted for the partial fulfillment of M.Sc. Final Examination in Applied Geology (2019) of Jadavpur University

Under the guidance of Prof. Nibir Mandal

Manjis Chanda

Examination Roll Number: MGEO194003

Registration Number: 128262 of 2014-15

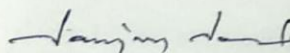**Department of Geological Sciences**

Jadavpur University
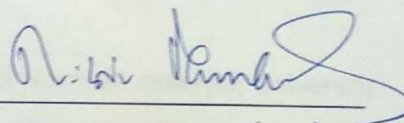
Kolkata-700032, India

2019

This is to certify that Sri Manjis Chanda has worked under my guidance and completed his thesis entitled **"Plume-Lithosphere interaction and its effect on surface topography: A theoretical and experimental approach"** in the Department of Geological Sciences, Jadavpur University. This thesis is being submitted towards the partial fulfillment of M.Sc. course in Applied Geology of Jadavpur University in the year 2019.

31.5.2019

Head of the Department,
Department of Geological Sciences
Jadavpur University
Kolkata

Head
Department of Geological Sciences
Jadavpur University
Kolkata-700032

Nibir Mandal   28/05/2019
Professor
Department of Geological Sciences
Jadavpur University, Kolkata

NIBIR MANDAL
Professor
Dept. of Geological Sciences
Jadavpur University
Kolkata - 700 032

Acknowledgements

I thank Professor Nibir Mandal for his persistent supervision, insightful suggestions and valuable discussions throughout the course of this dissertation. This thesis would not have been possible without his guidance and help.

I would like to acknowledge my seniors Dip Ghosh and Joyjeet Sen for their sincere guidance at every stage of this work. They have extended helpful inputs and suggestions which has allowed me to enhance my understanding of this thesis work.

I would like to thank my seniors Dr. Puspendu Saha, Manaska Mukhopadhyay, Giridas Maiti, Nandan Roy for their support during the course of this thesis work.

I also thank my classmate Rupsa Ray for her co-operation in the course of this project.

I would like to thank the Department of Geological Sciences, Jadavpur University for extending all possible support to me for the completion of this work.

Manjis Chanda

Abstract

Plumes are hot buoyant materials rising from the D'' layer in the lower mantle. When plumes hit the base of lithosphere, it forms a surface topography, lateral flow and lithospheric erosion. Lithospheric topography depends on viscosity, density of the buoyant plume material as well as on the rheological zoning in the lithosphere. In this thesis, the control of rheological parameters like viscosity contrast between plume and mantle is tested in physical experiments to understand the difference in dynamics of plume ascent and lithosphere interaction. Plume impinging the lithosphere generates under plating and surface topography. In order to quantitatively validate the result, Finite Element Modelling simulations are performed using ASPECT. The model also incorporates a rift zone in the lithosphere. Separation distance between plume axis and rift axis as well as rift velocity controls the ascent of plumes in lithospheric mantle. The viscosity of the plumes with respect to mantle in responsible for different morphology of plumes and different interactions. Lithosphere viscosity plays a crucial role in determining the type of lithospheric delamination. Maximum and minimum topography in an active rift zone is influenced by the plume impinging the base.

Contents

4. Physical modelling of Plume-lithosphere interactions

5. Plume-lithosphere interactions from finite element (FEM) modelling

Chapter 1

Introduction

1.1 Mantle plume hypothesis

The interior of the earth is composed of hot, dense, solid rocks shelled by a relatively thin and cooler crust. As the earth cools with time, the heat within the earth's core is transported outwardly through the mantle and crust. A thermal gradient exists between the successive compositional layers like the core mantle boundary allowing material to accumulate and subsequently rise as buoyant plumes, through the mantle, to the base of cold lithosphere. The stagnation of hot material at the base causes widespread melt generation within the lithosphere and eruption as basaltic magma to form Large Igneous Provinces (LIP). Mantle plumes during its ascent under the lithosphere, causes the lithosphere to swell with pronounced first order topography. The present thesis introspects this dynamic interaction between the lithosphere and the mantle plume through thermo-mechanical modelling.

 The term "hotspot" was first coined by Tuzo Wilson (1963a,1963b), where he envisioned a stable upwelling arm of the mantle convection as the source of

voluminous magmatic activities in LIPs, island-arc chains and stable upwelling in mantle. He proposed a fast moving plate moving over relatively slow moving source of melt produced fixed hotspots. Thus age progressive chains of islands (Hawaii etc.) are produced in the direction of plate motion. However, Wilson correlated hotspot volcanism with large scale convective patterns in mantle and constrained the source of melting to a depth of 200 Km. This hypothesis was later revised by Morgan (1971, 1981), suggesting hot plumes rising from deep mantle and spreading laterally across below the lithospheric plate as a source of hotspot magmatism. The fact that the geochemical signature of Ocean Island basalt volcanism was different and more primordial (compared to the more depleted signature of MORB volcanism rising from asthenosphere), led Morgan to conclude a deep source for OIB volcanism. He further recognized flood basalts as initial stages of plume volcanism, followed by a weaker stage relating to development of island chains.

This hypothesis lead to the development of theoretical, laboratory and numerical models on mantle plume dynamics. In the mantle, plumes are expected to develop as instabilities of thermal boundary layers (e.g. Parmentier et al. 1975; Loper and Stacey 1983). However, in vigorously convecting mantle such instabilities are transient features. Many of the early studies of mantle plumes focussed on the simpler case of an isolated laminar "starting plume" rising from a point source of buoyancy, a situation. Experiments Laboratory experiments performed using fluids with compositional buoyancy (Whitehead and Luther 1975; Olson and Singer 1985) and thermal buoyancy (Griffiths 1986a; Campbell and Griffiths 1990) led to the classical model of plumes with a bulbous "head" or "cavity" trailed by a narrow slender tail connected to the source. The development of instabilities in buoyant

layer of liquid overlain by dense ambient fluid was depended on the viscosity contrast between the fluids; where a lower viscosity of plume material lead to the formation of circular packets connected with the source through narrow tails (Whitehead and Luther 1975). When the viscosity of the plume material is high like mantle, plume heads must grow in size until the velocity of ascent is higher than the growth rate for liftoff. Olson and Singer (1985) showed that plumes with low viscosity contrast form narrow channels transporting material from source called "cavity" plumes. A more comprehensive approach was later on carried in laboratory experiments on the dynamics of isolated thermals and thermally starting plumes with the effect of temperature dependent viscosity (and density) (Griffiths 1986a, Coulliette and Loper 1995). Griffiths and Campbell (1990) investigated experimentally the dynamics of starting thermal plumes by injecting hot glucose syrup with a temperature excess into a cooler reservoir of the same fluid at a constant volumetric rate. They proposed that the growth of the plume head occurs with material supply from source as well as due to entrainment of ambient mantle. This results in a flattened, tortuous head described as "mushroom" shaped plumes. This classical plume model successfully explains the important features of several prominent hotspots, including the volume of the topographic swell (e.g. Davies 1988; Olson 1990; Sleep 1990) and the OIB, island chain volcanism (Olson and Singer 1985; Richards et al. 1989).

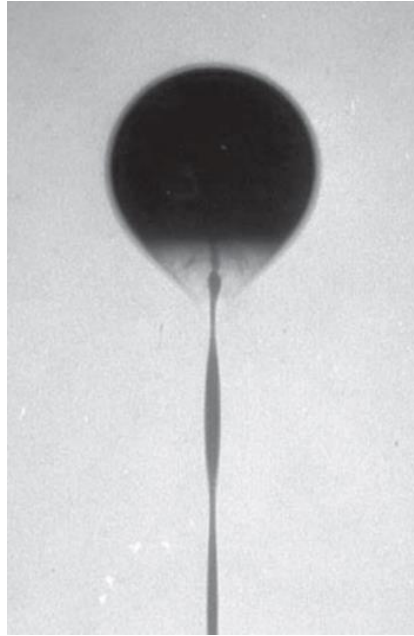Fig 1.1: Morphology of plumes from Olson and Singer (1985). (a) Diapiric plumes with low viscosity difference with surroundings, (b) Cavity plumes with high very high viscosity contrast.
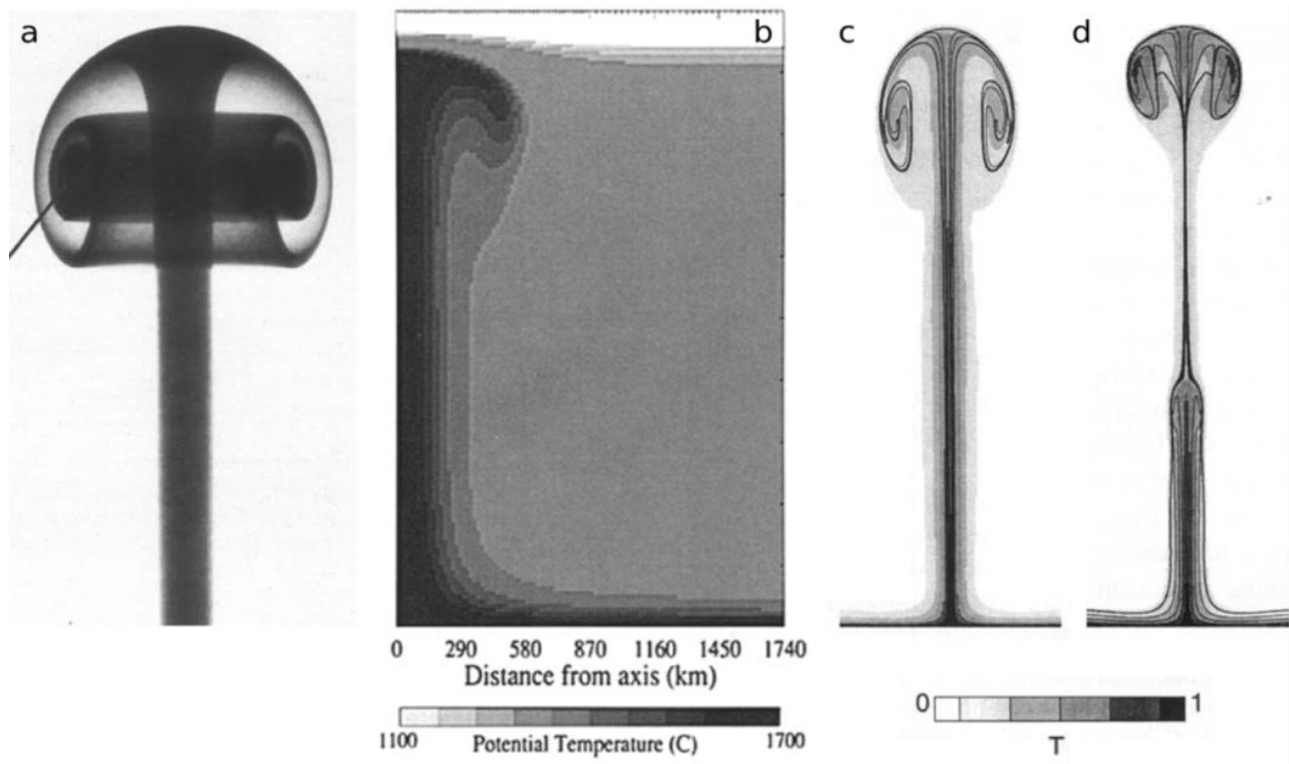

Fig 1.2: Classical Plume models: (a) Laboratory model of Griffith and Campbell (1990); (b) Numerical models of Fernentani Richards; (c) and (d) Numercial models of van Keken (1997) without and with stress dependent rheology respectively.

1.2   Description of lithospheric structure of globe

Alfred Wegener (1912), in his idea of "continental drift" proposed that rigid continental plates drifted like sledges on oceanic crust and positioned to the present configuration through time. However this was not widely accepted in the scientific community due to lack of mechanism that would push continents over large distances. It was not until seafloor spreading was documented via magnetic reversals on the ocean floor (Vine and Matthews, 1963; Vine and Wilson, 1965) that the theory gained traction and continues to evolve to this day.

 The main postulate of Plate tectonic was the outer layer of our planet is a rigid shell called 'lithosphere'. The layers are broken into mosaic of "plates" that are in motion. The deformation associated with these plates are concentrated along the boundaries of plates. Mainly three types of boundaries are defined in plate tectonics: divergent boundaries, convergent boundaries and transform fault. Divergent boundaries are characterized by the formation of new lithosphere; in transform fault two plates are sliding past each other and in convergent margin, the lithosphere is consumed by sinking into mantle through subduction processes or is thickened in mountain belt (e.g. Himalaya).

 Although lithosphere is loosely thought of as the outermost rigid layer of the earth, it is more precise to define in terms of the thermal and mechanical behavior. In case of oceanic lithosphere it is the outermost layer with conducting thermal gradient overlain by a convective adiabatic mantle. This is known as the thermal lithosphere (White 1988). Thus oceanic lithosphere is formed by the cooling of

underlying "asthenosphere". The part of lithosphere that bends under the application of load is elastic lithosphere, less than the thermal lithosphere.

Lithosphere consists of the crust and a part of upper mantle or lithospheric mantle. The earth's crust is bimodal distribution (oceanic and continental) depending on the thermal and mechanical properties. The continental crust varies in thickness between 30 km and 80 km, with an average thickness of 39 km (Christensen and Mooney, 1995). Although the continental crust represents only 0.57% of the mass of the silicate Earth, it represents over 60% SiO_2, 40% K, and 4.7% MgO (Hawkesworth and Kemp, 2006). It dominates the Earth's budget of incompatible and heat-producing elements such as U, Th and K (Taylor and McLennan, 2009). This extreme enrichment of incompatible elements in the upper crust came about due to intra-crustal melting and differentiation, and this process is also responsible for the stratification into felsic (granitic/granodioritic) upper crust and mafic (gabbroic/dioritic) lower crust (Condie, 1993). Due to its inaccessibility, the composition of the lower crust is less understood and one must rely on indirect methods to constrain its composition. These include (1) measurement of seismic velocities in the laboratory under appropriate temperature and pressure conditions; (2) by directly studying exhumed middle and lower crustal sections, and (3) by analyzing lower crustal xenoliths brought to the surface during volcanic eruptions. All of these approaches suggest that the lower crust is mafic in composition. The bulk composition of the continental crust is similar to arc-related intermediate rocks or andesites (Condie, 2012). The xenoliths and kimberlite provide information about the thermal gradient of the crust. The geothermal gradient in the upper 10Kms of the crust is high because of the presence of

radioactive elements contributing to the heat. The gradient gradually decreases in the lower part of lithosphere.
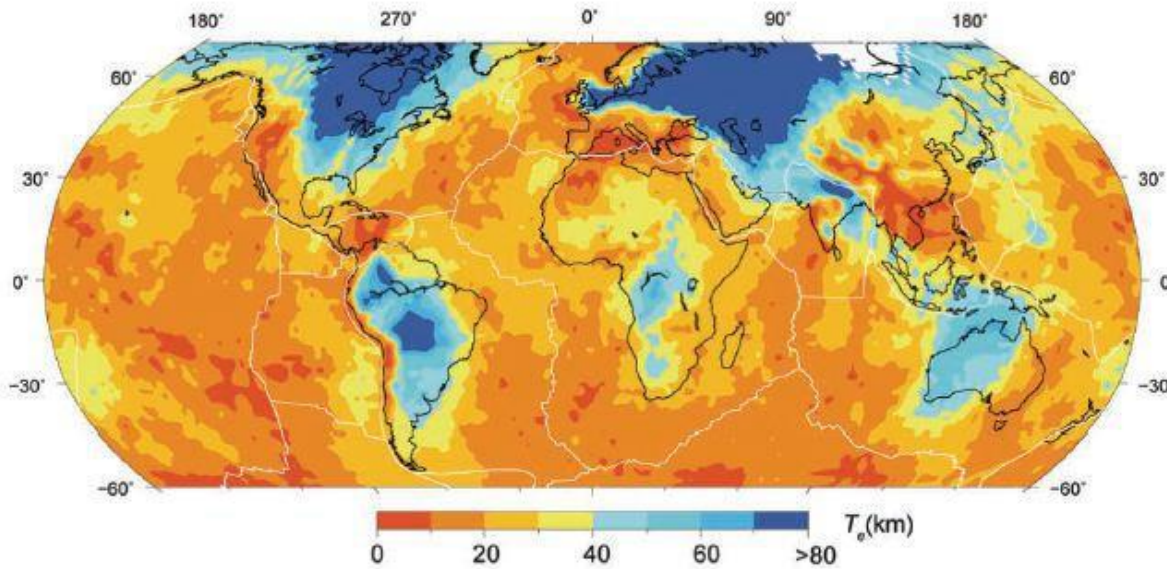
Fig 1.3: Global elastic thickness (Te) of the lithosphere (Mouthereau et al., 2013)
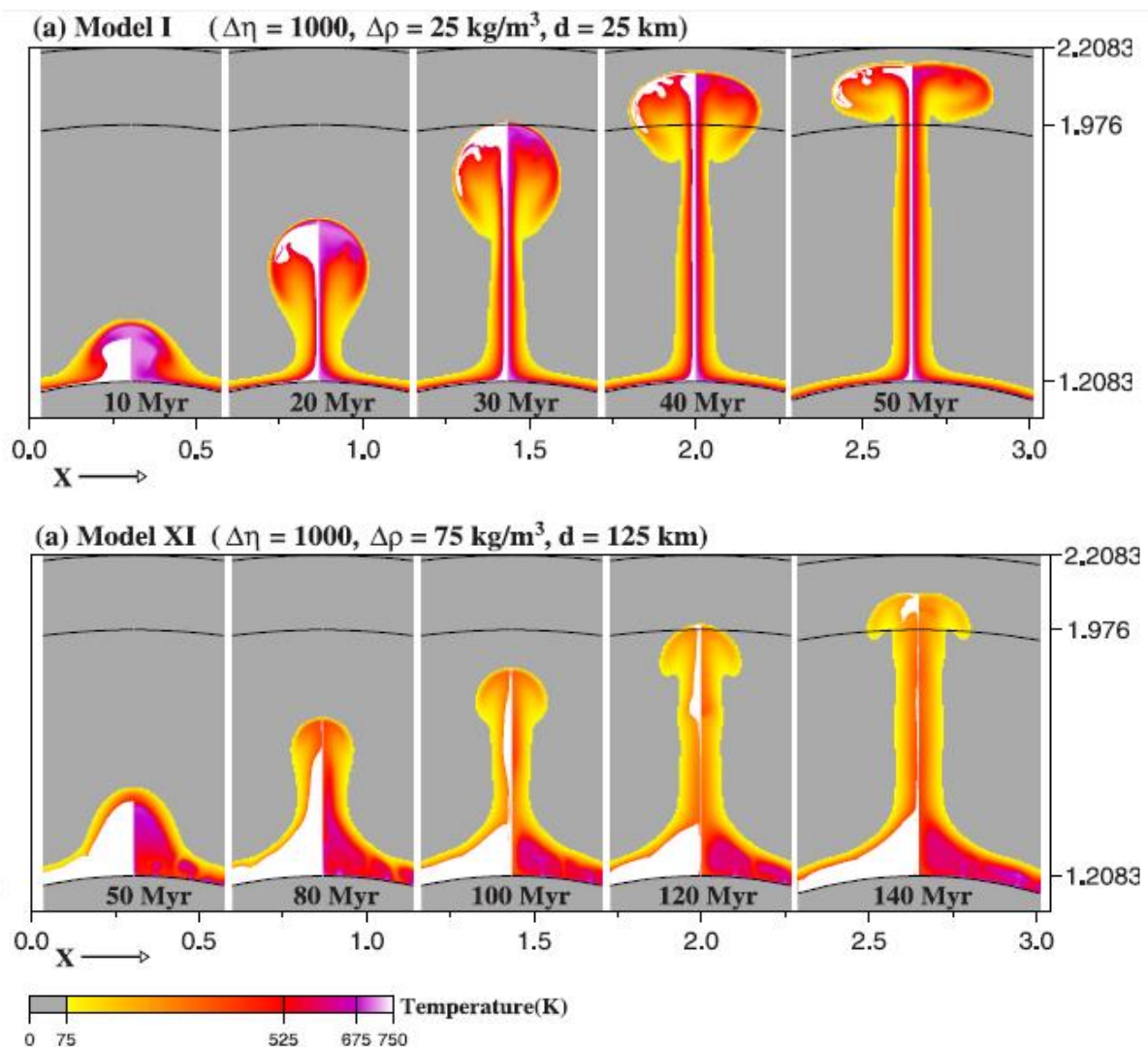
1.3   Plume Dynamics

Since the advent of classical plume concept, the new observations have led to the refinement of the theory. Numerical modelling and laboratory experiment helped to determine the boundary conditions, or material properties of plumes like density, viscosity while other models helped understand the feasibility of application in the earth's mantle. Studies on entrainment of dense layer suggest less than 10% entrainment during the ascent of the plumes (Fernentani and Richards 1995). Low temperatures compared to plume head, coupled with steady decrease of temperature in plume head, contributes to limited mixing of ambient material in finite depth of mantle. The evolution of geochemical signatures and chemical zonation inside a plume (Farnetani et al., 2002; Samuel and Farnetani, 2003; Farnetani and Hofmann, 2010; Li et al., 2014), the formation of plumes from

the top or the edges of thermo-chemical piles at the core–mantle boundary (Steinberger and Torsvik, 2012; Bower et al., 2013; Li et al., 2014), the influence of mantle rheology (Christensen, 1984a; Farnetani and Richards, 1995; Moore et al., 1999; Zhong et al., 2000; Lin and van Keken, 2006a; Lin and van Keken, 2006b) and phase transitions (Davies, 1995; Farnetani and Samuel, 2005; Leng and Zhong, 2010; Bossmann and van Keken, 2013), the surface expressions in comparison to regional geologic observations (d'Acremont et al., 2003; Leng and Zhong, 2010; Sobolev et al., 2011), plume–lithosphere interaction (d'Acremont et al., 2003; Sobolev et al., 2011; Ballmer et al., 2013; Burov and Gerya, 2014), influence on continental break-up (Burov and Gerya, 2014; Koptev et al., 2015), interaction with moving plates ing plates (Ribe and Christensen, 1994; Moore et al., 1998; Farnetani and Samuel, 2005; Ballmer et al., 2013; Agrusta et al., 2015) have also been studied.

Geochemical studies indicate that the source of plume material is heterogenous, chemically distinct component with respect to ambient mantle. Inclusion of this dense, less buoyant layer (compared to thermal plumes) in numerical models lead to different ascent dynamics in different dynamical regimes. Farnetani (1997) showed that plumes originating from a thermochemical boundary layer have decreased, more realistic excess temperatures than purely thermal plumes. Lin and van Keken (2005), Lin and van Keken (2006a), and Lin and van Keken (2006b) conducted numerical experiments attributing the parameters like temperature dependent viscosity, density contrast, thickness of the dense source thermal boundary layer (TBL) as controlling factors for plume morphology and entrainment. They find that in strongly temperature dependent viscosity cases, the chemical density difference plays a dominating role than thermal density. They identified three regimes: 1. Models with low density contrast (<40 Kg/m^3) and thickness of

TBL (<80 Km) showed classical plume shape with minimum entrainment. 2. The models where the density contrast is higher (>60 kg/m³) and thick layer (>80 Km) show substantial entrainment with voluminous topography at the base. 3. The regime with intermediate density difference and thickness shows a complex morphology with multiple pulses. Further work on the morphology of plumes due to interaction with phase boundaries, origin of plumes indicate a complex dynamical behavior of plumes in earth's mantle (Farnetani and Samuel ,2005; Kumagai et al. 2008 and Samuel and Bercovici,2006).

(a) Model I ($\Delta\eta = 1000$, $\Delta\rho = 25$ kg/m³, d = 25 km)

(a) Model XI ($\Delta\eta = 1000$, $\Delta\rho = 75$ kg/m³, d = 125 km)
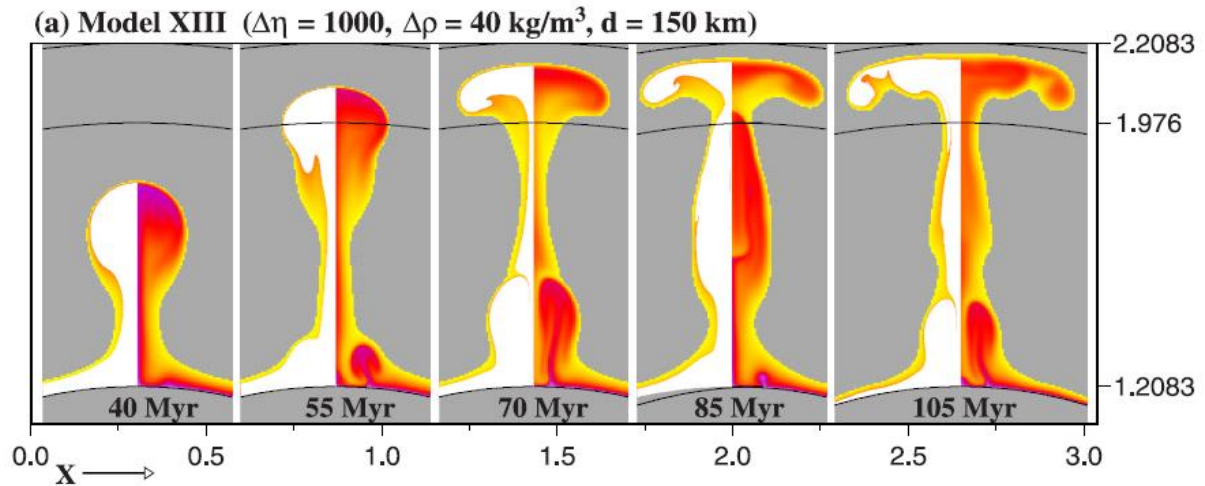
Temperature(K)

Fig. 1.4: Plume dynamics for temperature dependent viscosity (a) Cavity plumes for low density and low TBL layer thickness; (b) Plumes with a morphology at the base for high density contrast and high layer thickness (c) Pulsating Plumes with intermediate layer thickness. (After Lin and van Keken 2006a)

1.4 Plume-Lithosphere interaction

Since the direct evidence of Plume comes from the signature produced by the interaction of plumes with lithosphere, it is important to understand the dynamics of interaction. Plumes thermo-mechanically interact with lithosphere to produce hot-spot swells and in extreme cases breaking away of lithospheric plates. Initially (Olson and Nam, 1986) performed laboratory experiments of a rising low viscosity fluid deforming the upper high viscosity boundary layer, cooled from above to determine the amplitude of surface uplift with time. The typical evaluation comprised a three stage development, with initial rapid uplift followed by a phase of subsidence corresponding to stagnation and spreading off the plume material below the boundary layer. Griffiths and Campbell (1991) performed simpler experiments under isothermal conditions, and focused on determining scaling laws

10
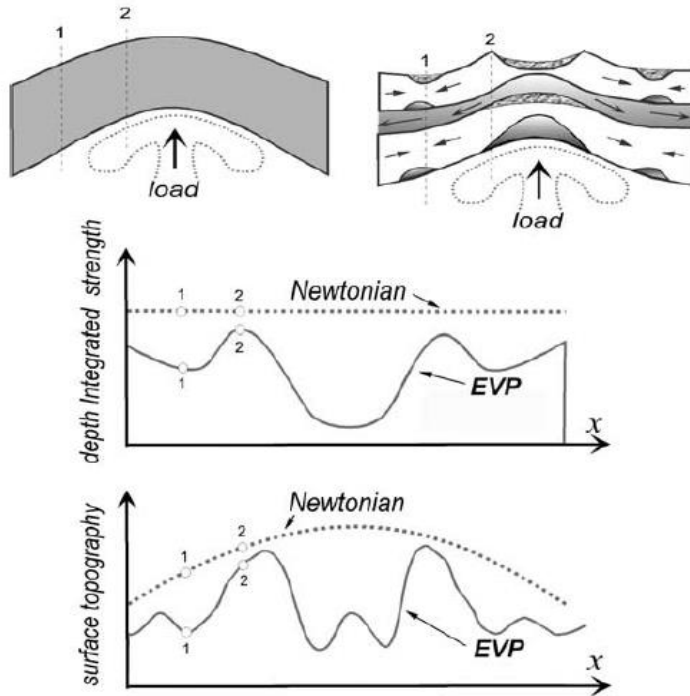
for the drop's radius and the thickness of the "squeeze film" above it as functions of time concluding similar outcomes. Moore et al. (1999) used a numerical model to study the interaction of an ascending thermal plume that impinges on cold, high-viscosity lithosphere at the surface of a fluid with strongly temperature-dependent viscosity. Results show that the boundary layer was subjected considerable amount of thinning when the viscosity contrast between the plume and ambient mantle exceeds 10, in contrast to the earlier models which showed little lithospheric thinning. However, Jurine et. al 2005 pointed out using numerical and laboratory simulations that depth of penetration is dependent on Buoyancy ratio, which is the ratio of density contrast due to composition to density contrast due to temperature difference between the plume head and mantle irrespective of temperature dependent viscosity. All these models considered the lithosphere as a viscous

Fig 1.5: Comparison between surface topography of Newtonian and Elastic-Viscous-Plastic rheology (after Gillou-Frottier, 2005)

boundary layer. However, close lithospheric studies indicate a complex elastic-brittle-ductile rheology with large scale deformations involving effects of lithospheric flexure. D'Acremont et.al, 2003; Burov and Gillou-Frottier, 2004, indicate that a layered rheology of lithosphere with a free surface are more sensitive to buoyant forces such that the ascent velocity of plumes is higher compared to the Newtonian rheology models. In order to explain the melting and lithospheric swells in Hawaiian plume, Ribe and Christenson, 1999 used "lubrication theory" to account for the spread of hot viscous material below a cold quasi-rigid moving lithospheric plate. This theory was used effectively for the theoretical analysis of plume–ridge interaction (Ribe et al.,1995; Ribe, 1996). The lateral extent of the spread of plume material in ridge-centred plumes increases with increasing volume flux of plume material and decreases with the increasing rate of ridge extension. Off-axis plumes, models (Ribe, 1996; Ito et al., 1997) predict that the primary controlling factor for the interaction is the self-spreading of the plume (in contrast to the slope of lithospheric thickness or thermal erosion of the lithosphere), and a distance between plume and ridge can be defined where plume flow towards the ridge and plate driven flow away from the ridge are balanced.
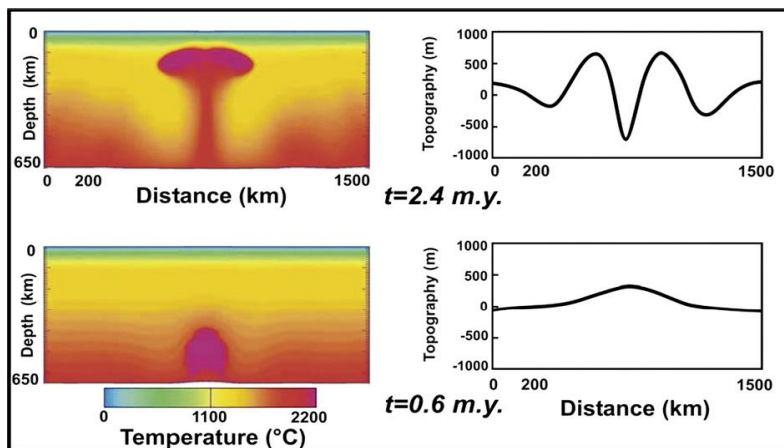

Fig 1.6 Numerical simulations for surface topography in E-V-P rheology (after Gillou-Frottier, 2005)
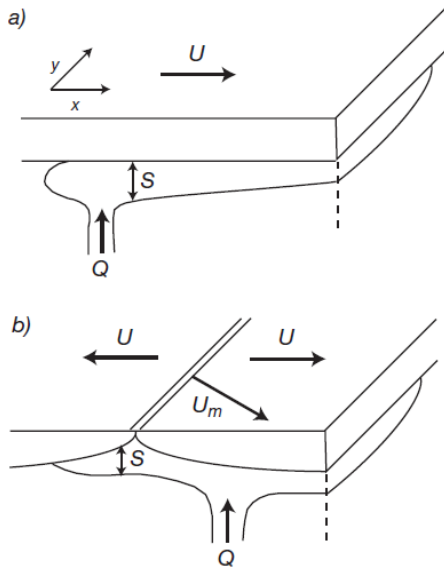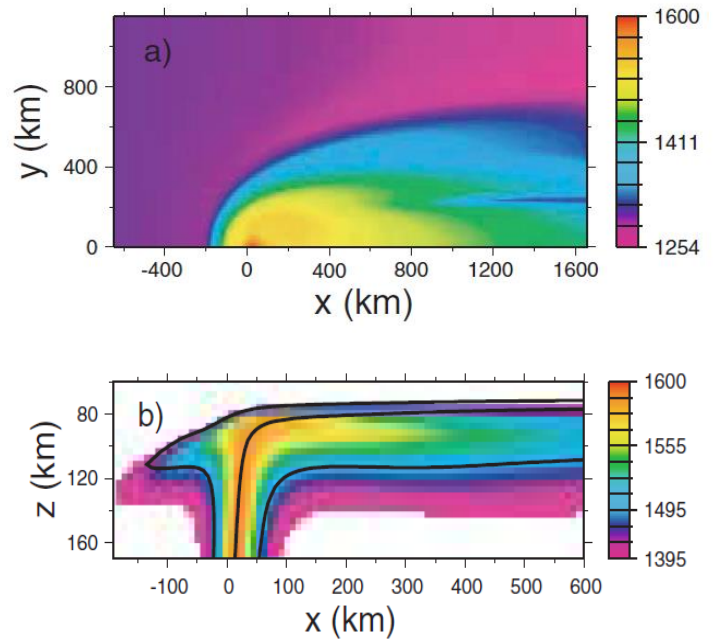
Fig1.7

Fig1.8

Fig 1.7: (a) Thin-layer model for plume-plate interaction. Buoyant plume fluid is released at a volumetric rate Q from a source fixed beneath a plate moving at speed U. The plume fluid is advected downstream by the moving plate as it spreads laterally, forming a layer whose thickness S(x, y) is much less than its lateral dimension. (b) Thin-layer model for plume-ridge interaction. The principle is similar to the plume-plate interaction model (a), except that the plume fluid is released near a mid-ocean ridge with half-spreading rate U that migrates at speed U_m relative to the plume.

Fig 1.8: Potential temperature (◦ C) for the reference Hawaiian plume model of Ribe and Christensen (1999). (a) horizontal plane at 110 km depth. (x, y) = (0, 0) is the center of the plume stem at 400 km depth. (b) vertical plane containing the plume symmetry axis. Black lines are trajectories of unmelted plume material.

1.5   Evidences of plume-lithosphere interaction

The plume-lithospheric interaction models essentially predicts large scale melting of the crustal material and formation of Large Igneous Provinces (LIP) and subsequent generation of island chains as the plate moves away from the source of melting (e.g. Richards et al., 1989). Coffin and Eldholm (1994) defined large igneous provinces as "massive crustal emplacements of predominantly mafic (Mg and Fe rich) extrusive and intrusive rock which originate via processes other than 'normal' seafloor spreading. So the source of melting must be different from that of the ordinary mantle material. The unique features include: (1) High areal extent and volume of magmatism, (2) Emplacement of large volume of magma within a geologically short range of time (with >75% of the total magma volume being emplaced in less than 1 – 5 Ma), (3) Unique geochemical, petrological, isotopic values. In many cases LIP volcanism precedes or is accompanied by rifting and continental breakup (e.g. Richards et al., 1989; White and McKenzie, 1989; Coffin and Eldholm, 1994; Ernst et al., 2005). The timing of LIPs has also been correlated with mass extinction events throughout the Earth's history (Courtillot and Renne, 2003; White and Saunders, 2005). Hotspots are surface expression of plume tails, characterized by the following features (Condie, 2001): (1) an active volcano present at the hotspot and an age progressive volcano in the direction of absolute plate motion, (2) A topographic swell of 500-1000 m, with a width of 1000-2000 kms, (3) An anomalous mass flux of 300 – 6300 kg/s (Steinberger, 2000).

 The temperature of the mantle plume head and tail can be estimated from the MgO and FeO contents, geochemical anomalies and excess uplift at the ridge due to plume buoyancy. Schilling (1990) investigated the plume temperatures and

constrained it to an excess temperature of 160-280 K. Herzberg and Gazel (2009), using MgO content compared the excess temperature of LIP and Ocean Island basalts with Mid Oceanic Ridge (MOR) basalts. They propose a higher excess melting temperature of 300 K for LIPs compared to younger OIBs. Mantle plumes are thought to have originated from the Core-mantle Boundary (CMB). CMB temperature ranges from 3300 – 4400K (Boehler, 2000; Hernlund et al., 2005; Lay et al., 2008), implying a 500- 1800 K temperature drop in plume head. This loss of temperature may be attributed to the adiabatic rise of mantle plumes through the mantle. However, adiabatic cooling or diffusion of heat cannot decrease the temperature to almost tenfold. Farnetani (1997) proposed that the the dense boundary layer in CMB could effectively decrease the temperature by restricting the entrainment to the hot material into the tail.

Geochemically LIP and OIBs have a characteristically different behavior compared to the other basalts. Comparative Spider diagram studies show that OIBs are enriched in incompatible elements and show a decline in abundance of trace elements with compatibility. MORB show a different trend of low incompatible elements with an increasing trend with compatibility. This difference in
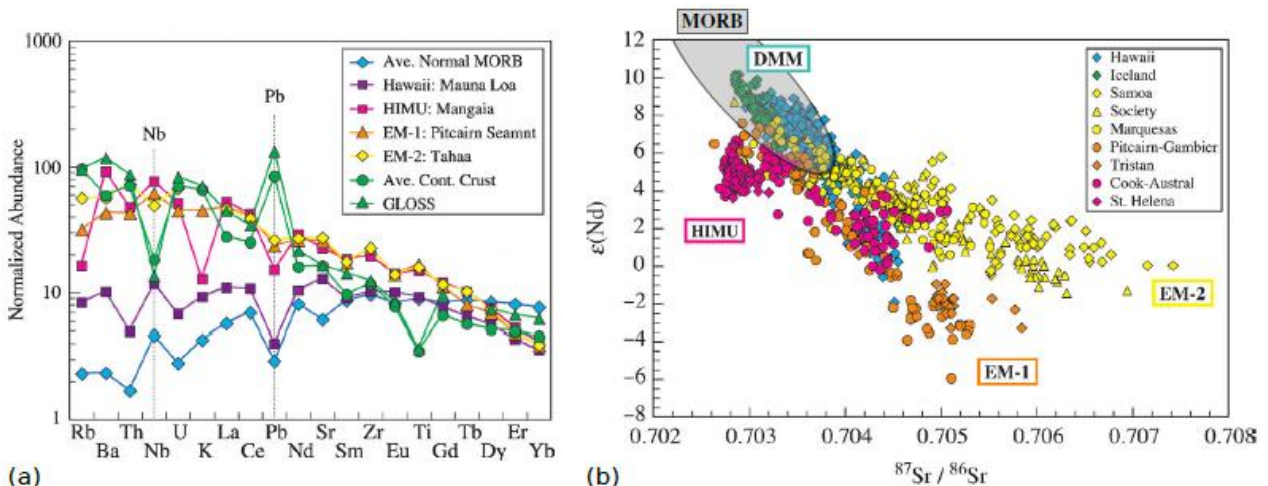
geochemical character may be attributed to the different sources of melting in mantle. ^{147}Sm/^{143}Nd and ^{87}Rb/^{87}Sr isotopic values are used to identify the characteristic mantle that had undergone melting. The values for OIB are quite different from that of MOR basalts indicating a geochemically enriched mantle (EM 1, 2) origin compared to the depleted mantle (DM) source of the former.
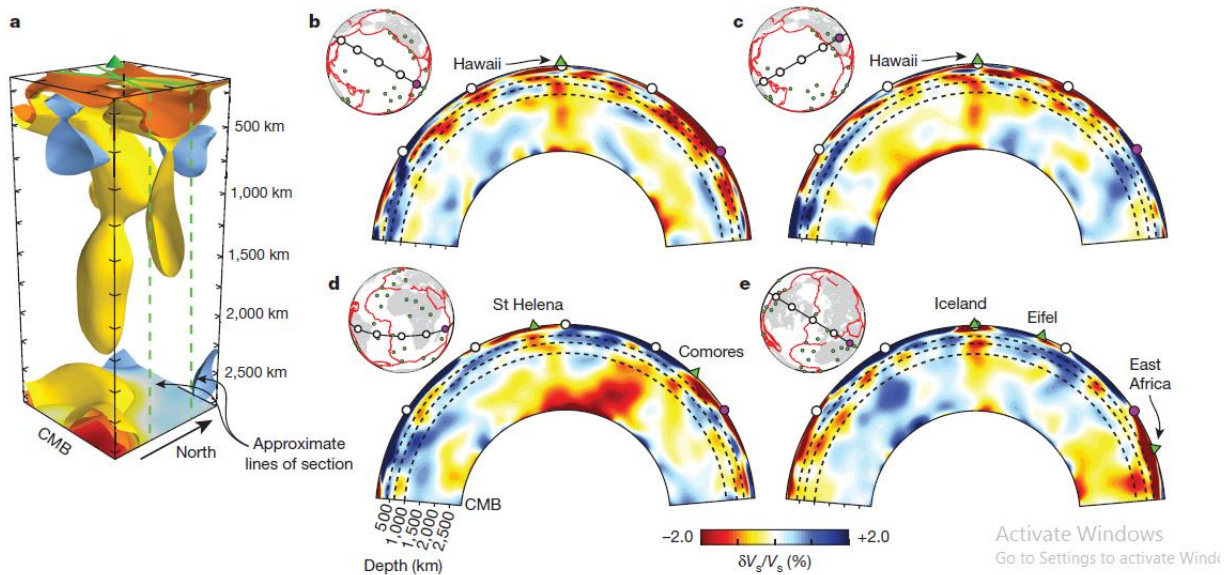

Fig 1.9: (a) Geochemistry of trace elements in MOR basalts and OIB. While OIB shows a decreasing slope with compatibility, the MOR basalts show opposite trend from Hofmann (2003).; (b) Stable isotope studies indicate Enriched Mantle (EM) origin for most of OIBs. Modified from Hofmann (2003).

Fig 1.10: Seismic tomographic images of mantle plumes, from French and Romanowicz (2015).(a) Three-dimensional rendering of the Hawaiian plume. (b-e) Two-dimensional vertical cross-sections, positions are indicated in the inset maps.

Although geochemical data provide an idea about origin and development of plumes, only Seismic investigations are capable of capturing the current thermal

state of the plumes. Identification of low seismic velocity anomalies in Plume tails imply a high temperature deep source of plumes in mantle. Regional and global studies have reliably revealed anomalies of low seismic velocities below ocean islands thought to originate from a mantle plume (Montelli et al., 2004; Wolfe et al., 2009; Rickers et al., 2013). French and Romanowicz (2015), who used advanced numerical techniques and included several different wave types in their model to achieve a better illumination also of the lower mantle. They show large, vertically continuous columns of low seismic velocities below major hotspots, reaching down to the CMB. Global tomographic models identified two antipodal ultra-low velocity (LLSVP) zones present in the lower mantle one under Africa, the other under pacific. These projected to the earth's surface correspond to the locations of LIPs and island chains. (Torsvik et al., 2006; Burke et al., 2008). This was interpreted as evidence that these LLSVPs or more specifically, their edges, are "Plume Generation Zones" which are stable for 100 Million years.

1.6 Overview

This thesis aims to study the response of surface topography due to the interaction of plume head with layered lithosphere. Scale down physical and numerical experiments are used to understand the control of parameters related to the plume on topographic responses. In Chapter 2, the basic Fluid mechanical theories have been discussed in detail. Chapter 3 contains he results of DEM and tomographic study of OIBs. Physical experimental setups and results are discussed in Chapter 4. Chapter 5 contains the results and the underlying models of numerical simulations performed using ASPECT. He results are summarized with conclusion and discussions in Chapter 6.

Chapter 2

Basic theory of fluid dynamics

2.1 Prologue

The present thesis deals geological systems under consideration as fluid media. This chapter gives a theoretical outline of the subject of fluid mechanics. Fluid dynamics describes the kinematic and dynamic relations of a fluid in framework of continuum mechanics using Newton's Laws of motion and thermodynamic principles. Fluid motion is described in terms of virus physical parameters like velocity v_i, pressure p , density ρ, in a particular time defined in a Eulerian or Lagrangian frame.

In Eulerian framework, fluid motion is defined by defining all properties as a function of space (x,y,z) and time (t). Thus information of flow is obtained at a single point varying with time. For example density variation with respect to time can be written as $\partial\rho/\partial t$, which is the local change in density or spatial derivative of density with respect to time obtained at a fixed location in space (x,y,z). To obtain the Total Derivative, the convective term must be added. Lagrangian approach on the contrary is "particle based approach", where the trajectory of individual particle is

tracked to understand the motion in the fluid. The density change can be expressed as Dρ/Dt, which is substantial derivative or material derivative. The Eulerian description is used commonly in hydrodynamic approach. However, when instantaneous properties of constitutive particles need to be understood Langrangian approach is useful.

The Lagrangian and Eulerian specifications of the kinematics and dynamics of flow is related by the substantial or material derivative. The acceleration of a fluid element may be attributed to two terms, the change in velocity with time at a particular location (local acceleration), and the change in velocity while moving to a new location (convective acceleration). In Eulerian frame, density field is described as ρ(*r, t*), where *r(x, y, z)* is a fixed location. Total derivative of density can be written as –

$$
\text{D}\rho/\text{D}t \;=\; \lim \delta t \to 0 \;\; \frac{\rho(\vec{r}+ \delta\vec{r}, t + \delta t) - \rho(\vec{r}, t)}{\delta t}
$$

$$
=\; \lim \delta t \to 0 \;\; \frac{\rho(\vec{x}+ \delta\vec{x}, \vec{y}+ \delta\vec{y}, \vec{z}+ \delta\vec{z}, t + \delta t) - \rho(\vec{x}, \vec{y}, \vec{z}, t)}{\delta t}
$$

$$
=\; \frac{\partial\rho}{\partial x}\frac{\partial x}{\partial t} + \frac{\partial\rho}{\partial y}\frac{\partial y}{\partial t} + \frac{\partial\rho}{\partial z}\frac{\partial z}{\partial t} + \frac{\partial\rho}{\partial t}
$$

$$
=\; \frac{\partial\rho}{\partial x} u + \frac{\partial\rho}{\partial y} v + \frac{\partial\rho}{\partial z} w + \frac{\partial\rho}{\partial t}
$$

$$
=\; \vec{u} \cdot \nabla\rho + \frac{\partial\rho}{\partial t} \qquad (2.1)
$$

Where ∇ is the differential operator and in Cartesian system expressed as

$$
\frac{\partial}{\partial x} i + \frac{\partial}{\partial y} j + \frac{\partial}{\partial z} k
$$

Similarly the acceleration can be expressed as :

$$\frac{D\vec{u}}{Dt} = \vec{u} \cdot (\nabla \vec{u}) + \frac{\partial \vec{u}}{\partial t} \qquad (2.2)$$

2.2 Conservation of Mass

In an enclosed space, the rate of change of mass is equal to the rate of change of fluid flow that happens across the volume. For an arbitrary volume

$$\frac{\delta \rho}{\delta x} \Delta x \Delta y \Delta z = \Delta y \Delta z ([\rho u]x - [\rho u]x + \Delta x) + \Delta z \Delta x ([\rho v]y - [\rho v]y + \Delta y + \Delta x \Delta y ([\rho w]z - [\rho u]z + \Delta z)$$

Dividing both sides by $\Delta x \Delta y \Delta z$, we get -

$$\begin{aligned} \frac{\partial \rho}{\partial x} &= -\frac{\partial \rho}{\partial x}(\rho u) - \frac{\partial \rho}{\partial y}(\rho v) - \frac{\partial \rho}{\partial z}(\rho w) \\ &= -\nabla \cdot (\rho \vec{u}) \\ &= -(\vec{u} \cdot \nabla \rho + \rho \nabla \cdot \vec{u}) \qquad (2.3) \end{aligned}$$

Further differentiating the products in Eq. (2.3) using Eq. (2.1),

$$\frac{D\rho}{Dt} = -\rho (\nabla \cdot \vec{u}) \qquad (2.4)$$

Equation (2.4) indicated that the change in density will be positive if the divergence of velocity field is negative or if flow tends to converge in element, it is the mass conservation equation For incompressible flows,

$$\frac{D\rho}{Dt} \; = \; 0 \qquad\qquad (2.5)$$

Hence, we have

$$\nabla \cdot \vec{u} \; = \; 0 \qquad (2.6)$$

2.2 Conservation of Momentum

The rate of change of momentum of a volume V bounded by surfaces that move with the flow are

$$\frac{d}{dt}\int_V dV \; (\rho\vec{v}) \; = \; \int dV \;\; \rho \, \frac{\partial\vec{v}}{\partial t} \quad (2.7)$$

Change of momentum in the fluid is due to the body forces as well as the the surface forces, hence we write –

$$Total\; force\; (\,body + surface) = \int_V dV\; (\rho\vec{g}\,) + \int_S [\sigma] \cdot d\vec{S}$$

$$= \int_V dV \ \{ (\rho \vec{g}) + (\nabla \cdot [\sigma]) \} \quad (2.8)$$

Equating 2.8 and 2.7,

$$\frac{D\vec{v}}{Dt} \rho = \rho \vec{g} + \nabla \cdot [\sigma] \qquad (2.9)$$

Eq. (2.9) is commonly described as *Equation of Motion*. Here $[\sigma]_{ij}$ is the stress tensor represented by nine components of stress. Considering the equilibrium of moments, it can be shown the stress tensor is symmetric, such that opposite diagonal components satisfy,

$$\sigma_{xy} = \sigma_{yx}, \ \sigma_{yz} = \sigma_{zy}, \ \sigma_{zx} = \sigma_{xz}$$

Some constitutive relation that correspond to the relation between stress and strain rate tensors are:

$$\sigma_{xx} = -p + \lambda \nabla \cdot \vec{v} + 2\mu \frac{\partial u}{\partial x}; \quad \sigma_{xy} = \mu \left(\frac{\partial v}{\partial x} + \frac{\partial u}{\partial y} \right) (2.10)$$

$$\sigma_{yy} = -p + \lambda \nabla \cdot \vec{v} + 2\mu \frac{\partial v}{\partial y}; \quad \sigma_{yz} = \mu \left(\frac{\partial v}{\partial z} + \frac{\partial w}{\partial y} \right) (2.11)$$

$$\sigma_{zz} = -p + \lambda \nabla \cdot \vec{v} + 2\mu \frac{\partial w}{\partial z}; \ \sigma_{zx} = \mu \left(\frac{\partial w}{\partial x} + \frac{\partial u}{\partial x} \right) \quad (2.12)$$

Where λ, μ are the coefficient of bulk and dynamic viscosity respectively. They express the stress vs. strain rate tensor for Linear (Newtonian fluids) and isotropic (inherent properties are same in all directions).

For incompressible flows ($\nabla \cdot \vec{v} = 0$), the general equation of (2.10-12) can be written as,

$$\sigma\, ij \;=\; -p\delta ij \;+\; \mu \left(\frac{\partial ui}{\partial xj} + \frac{\delta uj}{\delta xi} \right) \qquad (2.13)$$

Where u_i = (u, v, w); x_i = (x, y, z); δ_{ij} = Kronecker delta, δ_{ij} = 1 when i =j, δ_{ij} =0 when i ≠j.

Substituting Eq. 2.13 into Eq. 2.9, we have incompressible Navier-Stokes equation,

$$\frac{\partial u}{\partial x} + \frac{\partial v}{\partial y} + \frac{\partial w}{\partial z} = 0 \;\; (Eq.\, of\, continuity)$$

$$\rho \frac{Du}{Dt} \;=\; \rho gx - \frac{\partial p}{\partial x} \;+\; \mu\,(\, \partial 2u\,/\,\partial x2\, +\, \partial 2u\,/\,\partial y2\, +\, \partial 2\, u\,/\,\partial z2 \,) \quad (x\, component)$$

$$\rho \frac{Dv}{Dt} \;=\; \rho gy - \frac{\partial p}{\partial y} \;+\; \mu\,(\, \partial 2v\,/\,\partial y2\, +\, \partial 2v\,/\,\partial y2\, +\, \partial 2\, v\,/\,\partial z2 \,) \quad (y\, component)$$

$$\rho \frac{Dw}{Dt} \;=\; \rho gz - \frac{\partial p}{\partial z} \;+\; \mu\,(\, \partial 2w\,/\,\partial w2\, +\, \partial 2w\,/\,\partial y2$$
$$+\, \partial 2\, u\,/\,\partial z2 \,) \quad (z\, component)$$

$$\rho\, D^2\vec{v}/Dt = \rho\vec{g} - \nabla p + \mu\, \nabla^2\vec{v} \qquad (2.14)$$

Eq. 2.14 represents the general form of Navier- Stokes equation, where ∇^2 is the Laplacian operator.

2.4 Conservation of energy

The two main process of transportation are conduction and convection. While conduction is the main process of transport in the crust or lithosphere, convection is the main mechanism of heat transfer in the earth's mantle. The basic aw of heat conduction is known as the Fourier law of heat transfer:

$$q = -k\frac{\partial T}{\partial x} \qquad (2.15)$$

Where k is the thermal conductivity.

Energy equation can be expressed as –

$$\rho\left[\frac{\partial h}{\partial t} + \nabla \cdot (h\vec{v})\right] = \frac{D\rho}{Dt} + \nabla \cdot (k\nabla T) + \varphi \qquad (2.16)$$

Where h is the specific enthalpy, T is the absolute temperature. K is the thermal conductivity of the fluid. Dissipation function is represented by ϕ signifies the work done against viscous forces.

2.5 Stokes flow

The density of a fluid body decides whether another body of high viscosity will rise or sink through it. If the second body has a higher density it will sink, and if the density is lower than the medium it will rise due to the force of buoyancy. The flow is also influenced by the viscous forces (F_d). If the velocity of a spherical body of radius R is V in a fluid of viscosity μ, then according to *Stokes law*,

$$F_d = 6\pi\mu RV \quad (2.17)$$

Reynolds number (Re) depends on the viscosity and the velocity of the body that moves through the fluid. In case of high viscosity, the Re will be very small with negligible inertial forces. The velocity of the body is reduced, and the kind of flow is known as Stokes flow. For viscous system, force balance of the body gives the kinematic solution to such flows. The forces acting on the body being its own weight (mg), buoyancy force (F_b) and drag force (F_d) when balanced gives,

$$F_b + F_d = mg$$

$$4/3\ \pi R^3(\rho_{fluid})g + 6\pi\mu RV = mg = 4/3\ \pi R^3 \rho g \quad (2.18)$$

Where ρ_{fluid} is the viscosity of the ambient fluid, ρ is the viscosity of mass m rising through the fluid.

2.6   Theory of Rayleigh-Taylor instabilities

The term instability refer to the internal component that grows to achieve equilibrium in the system. In a system where two layers of fluids with different density, generally the heavier fluid overlain by the lighter fluid, the Rayleigh Taylor Instability (R-T instability) grows at the interface between two fluids. Both gravity and buoyancy forces act as driving forces. With the formation of R-T instability at the interface, pockets of the lighter fluids rise upward after a certain interval of time with an equal amount of heavier fluid coming down to fill it's space. The growth of the instability decreases the potential energy of the system as the heavier liquids sinks.
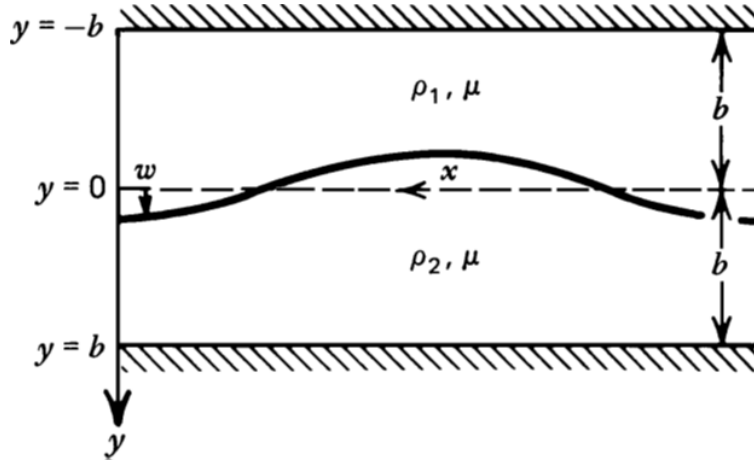
Fig. 2.1: The Rayleigh-Taylor Instability at the interface between a lighter fluid overlain by a denser fluid.

If instability starts to grow in a horizontal layer of thickness b, then vertical displacement of the interface (w) can be written as,

$$w = w_o \cos\frac{2\pi x}{\lambda} \qquad (2.19)$$

where λ is the wavelength and $w \ll \lambda$. Turcotte and Schubert (2002) in used R-T instability in their experiment. If there are two horizontal parallel fluid layers of equal thickness (b) and equal viscosity (μ) with densities (ρ_1 and ρ_2, where $\rho_1 > \rho_2$). Boundary of the undisturbed interface, lower and upper boundaries at y = 0, +b, -b respectively.

The equation for stream function (ψ) yield,

$$\Psi = \sin\frac{2\pi x}{\lambda}\left(Ae^{-2\pi y/\lambda} + Bye^{-2\pi y/\lambda} + C\,e^{2\pi y/\lambda} + Dye^{2\pi y/\lambda} \right) \qquad (2.20)$$

Writing the same equation in terms of hyperbolic functions, for upper layer and lower layer respectively are,

Ψ_1 = sin 2πx/λ { A1 cosh(2πy/λ) + B1 sinh(2πy/λ) + C1y cosh(2πy/λ) +

D1y sinh(2πy/λ)} $\qquad$ (2.21)

Ψ2 = sin 2πx/λ { A2 cosh(2πy/λ) + B2 sinh(2πy/λ) + C2y cosh(2πy/λ) +
D2y sinh(2πy/λ) $\qquad$ (2.22)

The velocity components in terms in terms of stream function are

$$u = - \partial\psi/\partial y \quad and \quad v = \partial\psi/\partial x \qquad (2.23)$$

Differentiating the stream functions to obtain velocity components as,

$$u1 = - \frac{2\pi}{\lambda} \sin(\frac{2\pi x}{\lambda}) \ \{ \ (A1 + C1y + \lambda \frac{D1}{2\pi}) \ \sinh (\frac{2\pi y}{\lambda}) + (B1 + D1y + \lambda \frac{C1}{2\pi}) \cosh \frac{2\pi y}{\lambda} \}$$

(2.24)

$$u2 = - \frac{2\pi}{\lambda} \sin(\frac{2\pi x}{\lambda}) \ \{ \ (A2 + C2y + \lambda \frac{D2}{2\pi}) \ \sinh (\frac{2\pi y}{\lambda}) + (B2 + D2y + \lambda \frac{C2}{2\pi}) \cosh \frac{2\pi y}{\lambda} \}$$

(2.25)

$$v1 = - \frac{2\pi}{\lambda} \cos(\frac{2\pi x}{\lambda}) \ \{ \ (A1 + C1y) \ \cosh (\frac{2\pi y}{\lambda}) + (B1 + D1y) \sinh \frac{2\pi y}{\lambda} \}$$

(2.26)

$$v2 = - \frac{2\pi}{\lambda} \cos(\frac{2\pi x}{\lambda}) \ \{ \ (A2 + C2y) \ \cosh (\frac{2\pi y}{\lambda}) + (B2 + D2y) \sinh \frac{2\pi y}{\lambda} \}$$

(2.27)

For evaluating the constants of integration, boundary conditions of no slip and continuity of u, v across the interface is used. For no slip condition at y = + - b, we need for u1 = v1 = 0 at y = -b and u2 = v2 = 0 at y = b. For small displacement,

continuity holds in the interface such that u1 = u2 and v1 = v2 at y =0. By applying the boundary conditions in eq. 2.24 to 2.27 the stream function is written as,

$$\Psi1 = A1 \sin\left(\frac{2\pi x}{\lambda}\right) \cosh\left(\frac{2\pi y}{\lambda}\right) + A1 \sin\left(\frac{2\pi x}{\lambda}\right\{ \frac{y}{b}\left(\frac{\lambda}{2\pi b}\right) \tanh\left(\frac{2\pi b}{\lambda}\right) \sinh\left(\frac{2\pi y}{\lambda}\right)$$

$$+ \left(\frac{y}{b}\cosh\left(\frac{2\pi y}{\lambda} - \frac{\lambda}{2\pi b}\sinh\frac{2\pi y}{\lambda}\right) \quad X \quad \left(\frac{\lambda}{2\pi b} + \frac{1}{\sinh\left(\frac{2\pi b}{\lambda}\right)\cosh\left(\frac{2\pi b}{\lambda}\right)}\right)$$

$$X \quad \left\{\frac{1}{\sinh\left(\frac{2\pi b}{\lambda}\right)\cosh\left(\frac{2\pi b}{\lambda}\right)} - \left(\frac{\lambda}{2\pi b}\right)^2 \ \tanh\frac{2\pi b}{\lambda}\right\}^{-1} \qquad (2.28)$$

The expression for Ψ2 is obtained by replacing y by −y in eq. 2.28, we obtain equation of interface. The rate of change of displacement of the interface (∂w/∂t) is equal to the vertical component of velocity. Differentiating (2.28) the vertical velocity can be calculated as:

$$\frac{\partial w}{\partial t} = \frac{2\pi A1}{\lambda} \cos\frac{2\pi x}{\lambda} \qquad (2.29)$$

Since the fluid of density ρ1 replaces the fluid of density ρ2, additional weight of the fluid (ρ1 - ρ2)gw is felt as normal stress or pressure on the distributed interface. It must be balanced by net normal stress due to viscous stress and flow pressure.

$$\frac{\partial w}{\partial t} = \frac{w}{\tau} \qquad \text{where τ is the growth time of a disturbance.} \qquad (2.30)$$

Finally solving the equation of τ we get,

$$W = w_o \, e^{\, t/\tau} \qquad (2.31)$$

Value of τ depends on the wavelength λ of the interface between two fluids. For unstable configuration (ρ1>ρ2), the disturbance with shortest time constant grows and dominated the instability. Wavelength λ = 2.568b gives the smallest value of τ. Therefore,

$$\tau = (13.04\mu)/ (\rho1-\rho2)gb \qquad (2.32)$$

The instability takes longer time to grow for more viscous fluids when the density contrasts smaller. (Details in Turcotte and Schubert 2002).
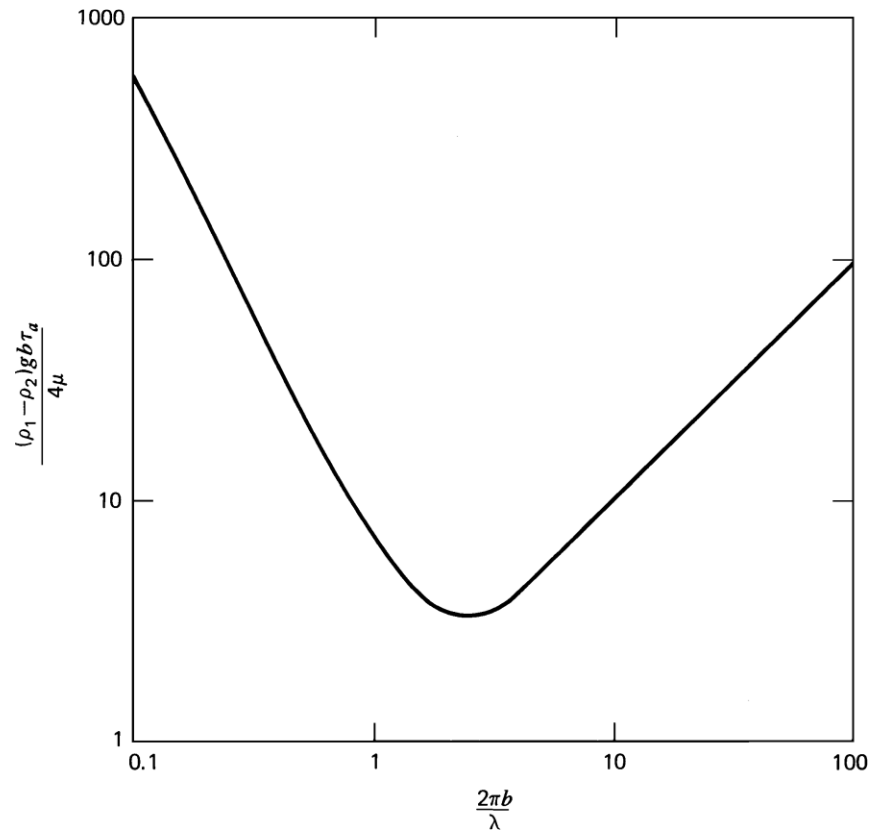
Fig. 2.2: Dimensionless growth time as a function of dimensionless wave number for Rayleigh-Taylor instability. Adapted from Turcotte and Schubert 2002

2.7 Theory of thermo-mechanical instabilities

Thermo-mechanical instabilities are develop due to change in properties of materials with changing temperature. Rayleigh-Benard convection is a type of natural convection process which occurs as a consequence of thermo-mechanical instabilities trying to achieve thermal and mechanical equilibrium.

If $\rho 1$ denotes the density at the bottom (temperature T1) and for a small temperature difference between top and bottom boundary layers we write

$$\rho_o = \rho_1 [1 - \alpha(T1-T2)],$$

where α is the coefficient of volume expansion. So the thermal gradient density becomes

$$\Delta \rho = \rho_o - \rho_1 = -\rho_1 \alpha (T1 - T2) \tag{2.33}$$

When temperature difference sets some critical value (ΔTcr), energy transfer through reorganization of hot and old fluids become more efficient than thermal and viscous dissipation, fluid motion sets in. Rayleigh number ($Racr$) represents the relation between gravitational forces, viscous forces and buoyancy forces. When $Racr$ reaches 1708. Instability sets in and convection cells appear.
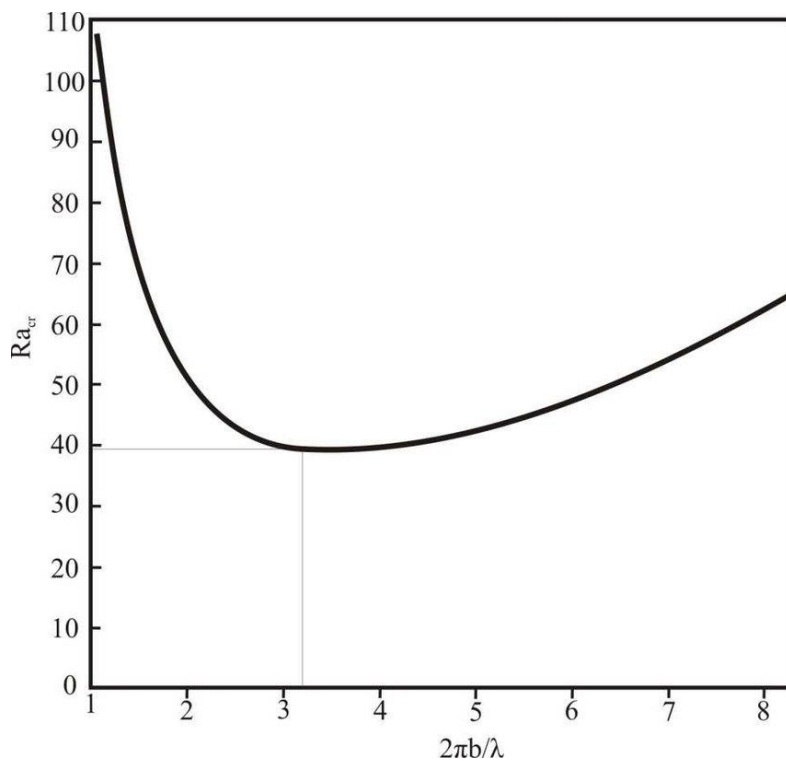
Fig. 2.3: Critical Rayleigh number $Racr$ on the onset of convection in a laye heated from below with no slip at the boundaries with respect to wavenumber $2\pi b/\lambda$

Chapter 3

Plume-lithosphere interactions: an analysis from DEM and seismic tomography

3.1 Approach

The surface topography of the lithosphere is generally formed due to the horizontal tectonic forces operating on the plate boundaries. However, intra-plate lithospheric swells are formed, which cannot be explained due to the tectonic stress. Rather the mantle flows are held responsible for this kind of topography called "Dynamic topography". Mantle plumes are produced deep within the lower mantle D" layer. When it reaches the surface, it pushes the lithosphere and produces a topographic swell on the lithosphere. Studies conducted in laboratory studies show a staged development of this surface topography, where initially it rises to a maximum height followed by subsidence due to lateral spreading of plume head below the lithosphere (Olson and Nam 1986, Griffith et. al 1989). The height and width of the swell depends on the density anomaly and diameter of the plume head. With gradual subsidence the early Gaussian swell is followed by a flattened plateau. Initially the height may reach upto 500-1000m, with a thickness of about 2000Kms. Due to subsidence it forms a plateau with reduces height with

swell thickness of 2000Km. The rate at which the subsidence occurs depend on the viscosity of the lithosphere ($3x10^{20}$ Pa-s). However later numerical models predict that the topography of the lithosphere is also influenced by the isostatic adjustments and vertical layering specially within continental lithosphere. (d'Acremont 2003, Burov and Frottier 2005). The various first order surface topography over hotspots around the world is studied using Digital Elevation Models (DEM). Seismic tomographic images under these hotspot swells are also analysed in order to understand the morphology of buoyant plumes and their origin in mantle

3.2 DEM Analysis

Digital Elevation models (DEM) measures the surface topography at a particular section. Topographic profiles are analyzed from the DEM images to understand the morphology of lithospheric swells in continental and oceanic crusts. Only first order topography is considered during the analysis, while lower orders are neglected. Continental hotspots (eg. Afar, Africa) shows swells with amplitude of 2000mts and width of 1700m. The height of the surface topography in oceanic crust are similar and ranges from (1500-2000mts) but the width of the swell varied ranging from 350 –1000 mts at different locations. Another interesting observation from Galapagos and Hawaii hotspot swells are that formation of depressions on either side of the topographic swell. Plume induces topography can be difficult to interpret because topography are associated with erosion which reduces the topography formed by plumes. Even if the erosion rates are estimated, isostatic adjustments may further reduce the topography.
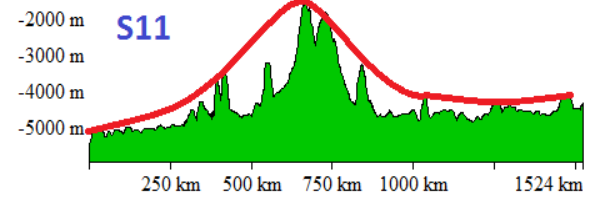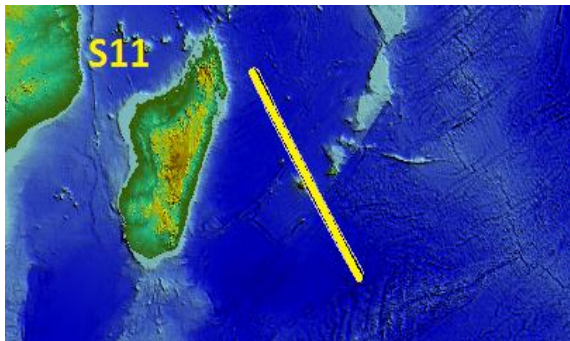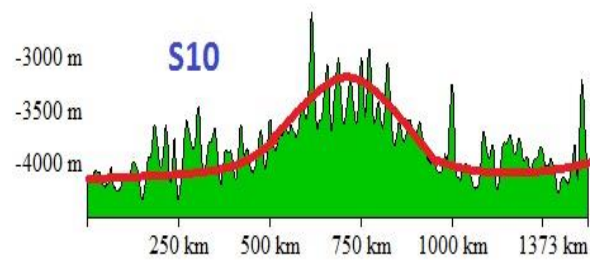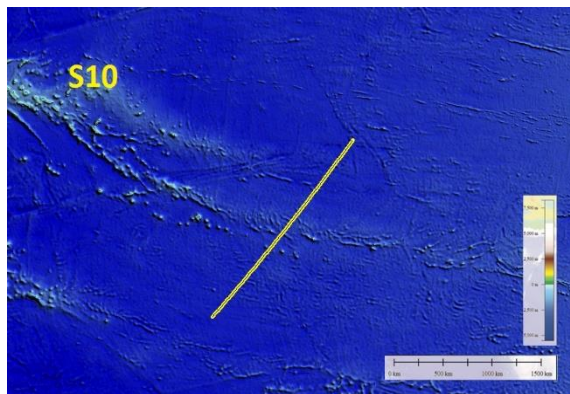
34
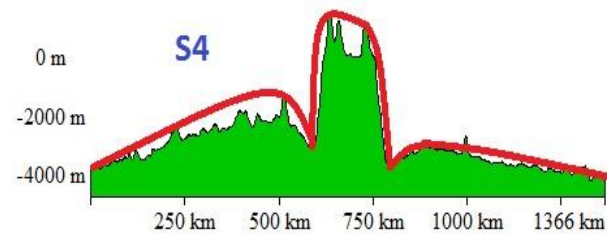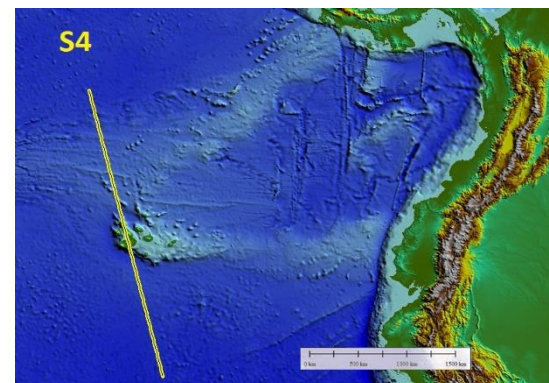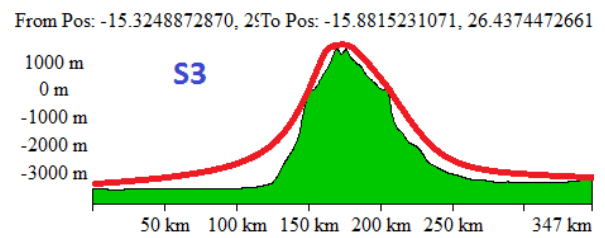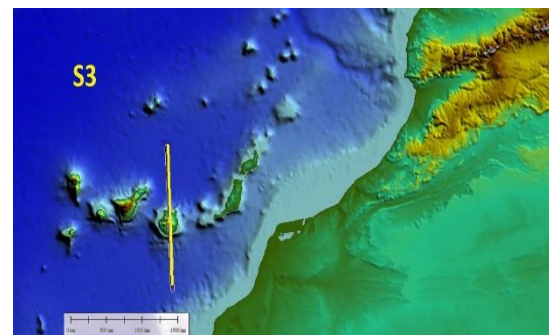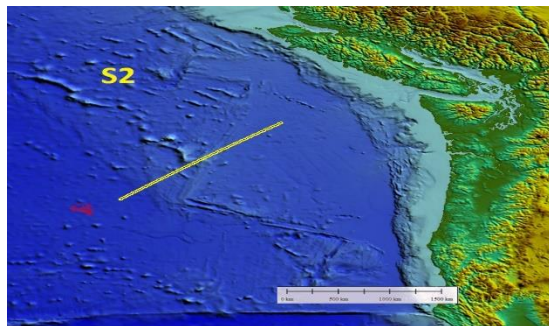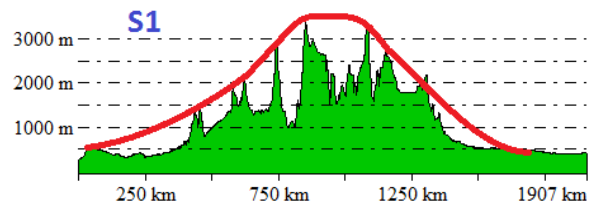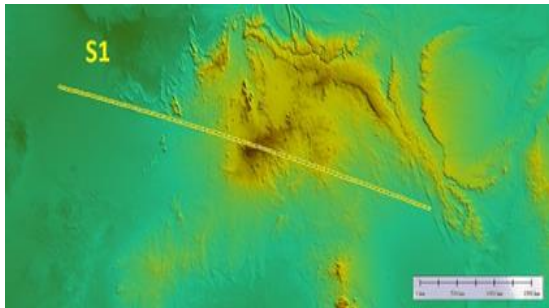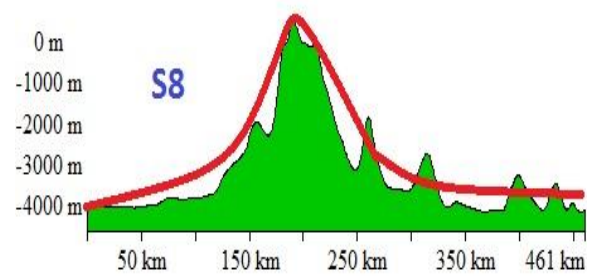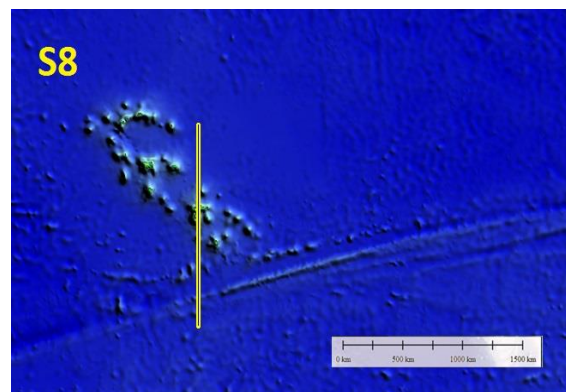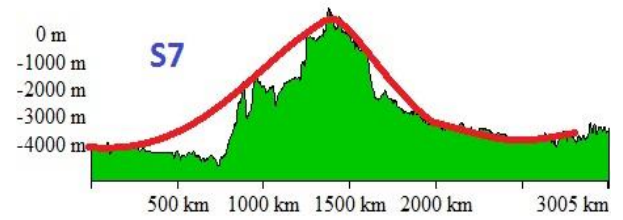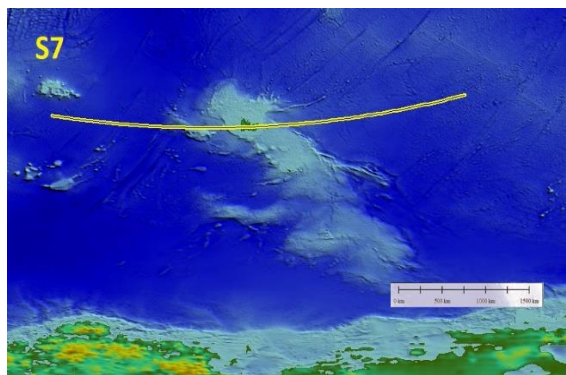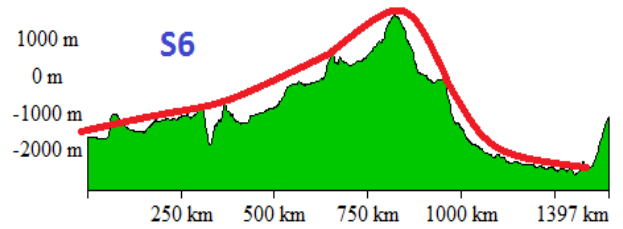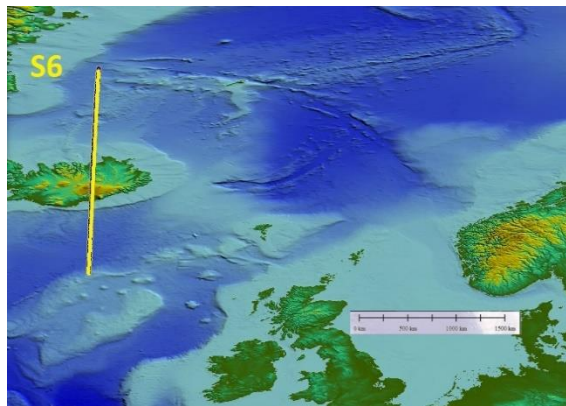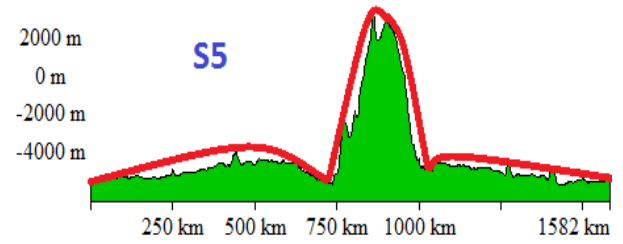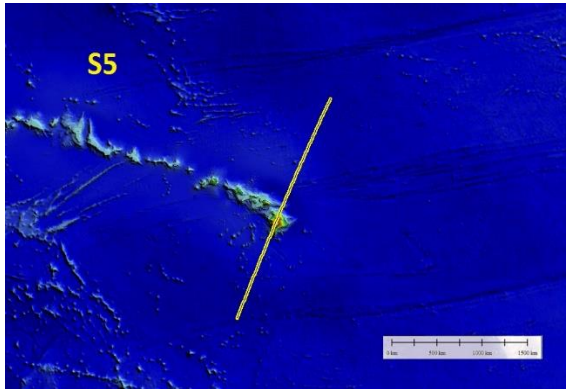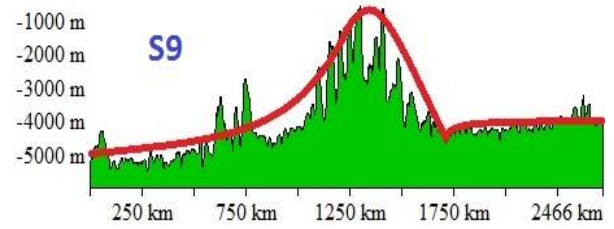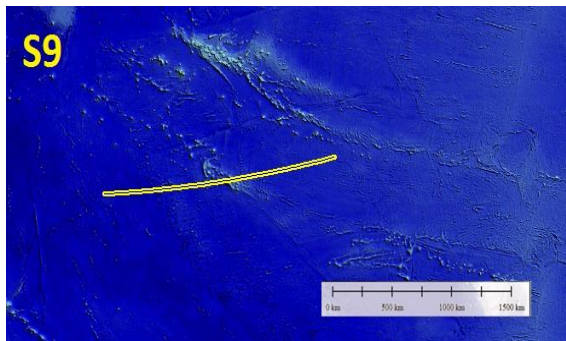
Fig 3.1: DEM sections and corresponding surface topography of lithospheric swells at hotspot locations: Afar (S1), Cobb (S2), Canary (S3), Galapagos (S4), Hawaii (S5), Iceland (S6), Kerguelen (S7), Marquesas (S8), McDonald (S9), Pitcairn (S10), Reunion (S11)

3.3 Seismic tomography analysis

Although laboratory experiments and numerical models indicate a deep origin of mantle plumes explains the distinct isotopic signature of flood basalts and lithospheric swells, direct evidences have been lacking until the seismic tomography analysis was done under the hotspots. Here, in this chapter, the mantle tomographic depth sections under hotspots were investigated to understand the origin and morphology of mantle plumes using PRI-P05 model for P-waves (Montelli et. al 2004). Seismic P wave velocity travel times are recorded in seismographs during an earthquake all over the surface of the earth. Ideally in a spherically symmetric earth model it is assumed that the P waves have an average velocity in a certain layer of mantle, where the chemical and physical properties are consistent. However, travel times recorded show a deviation from the calculated times, known as travel time residuals or anomalies. Since seismic velocities are dependent on physical properties like density and elastic moduli of the layer, which vary with temperature inside earth. So anomalies are interpreted to be fluctuations in temperature in mantle, where regions of fast traveling waves are interpreted to be cold domains while lower than average anomaly indicates a high temperature zone. Generally columnar low velocity anomalies in tomographic sections are interpreted as mantle plumes. In this chapter, tomographic sections under hotspots are analyzed. (Source: submachine.com). Most mantle plumes show a lower mantle origin ranging from 1000-2800 Km. (Table 3.1). Afar hotspot shows a deep mantle origin. While other Iceland, Galapagos, Cobb show upper mantle origin below 670 Km boundary. Although laboratory experiments indicate narrow plumes, tomography images point out thicker plumes (~300Km avg.).
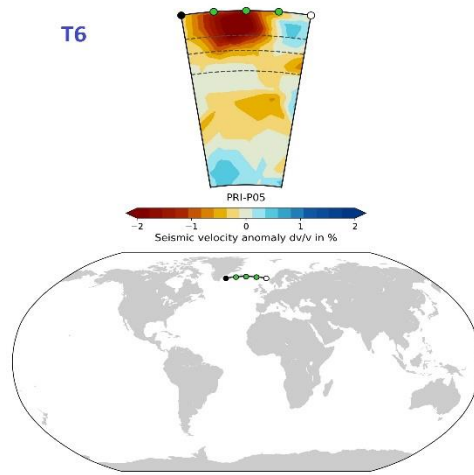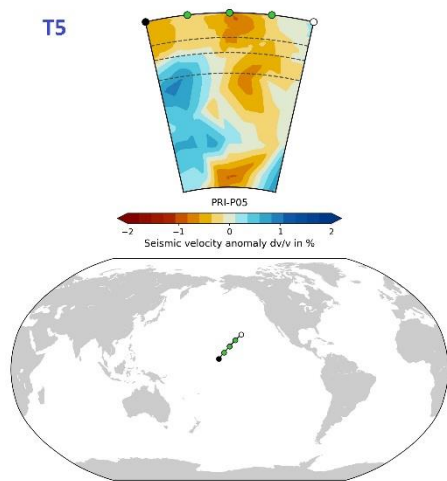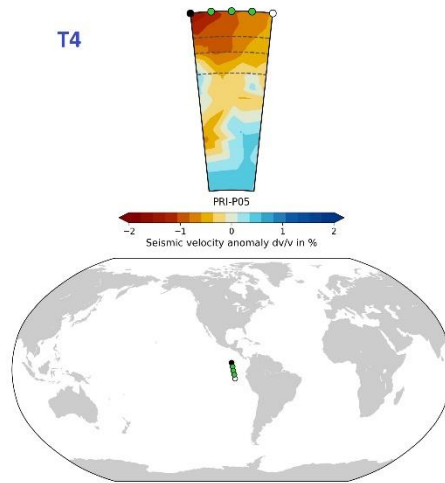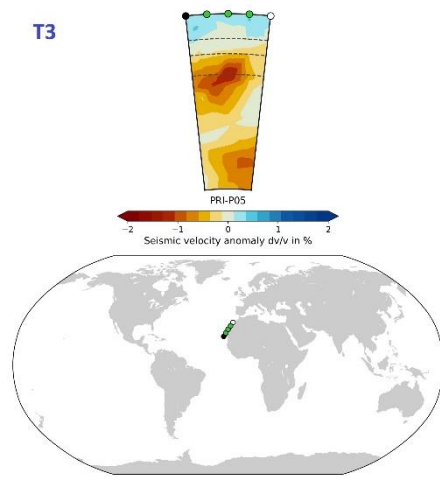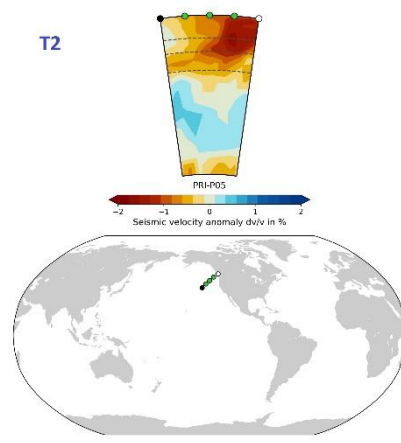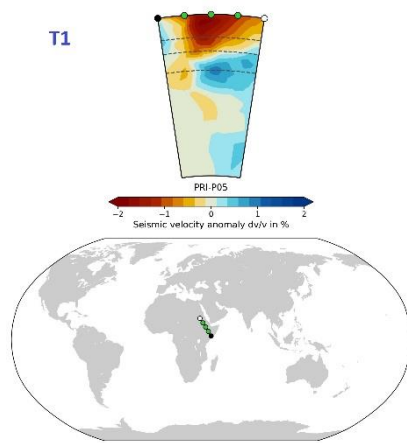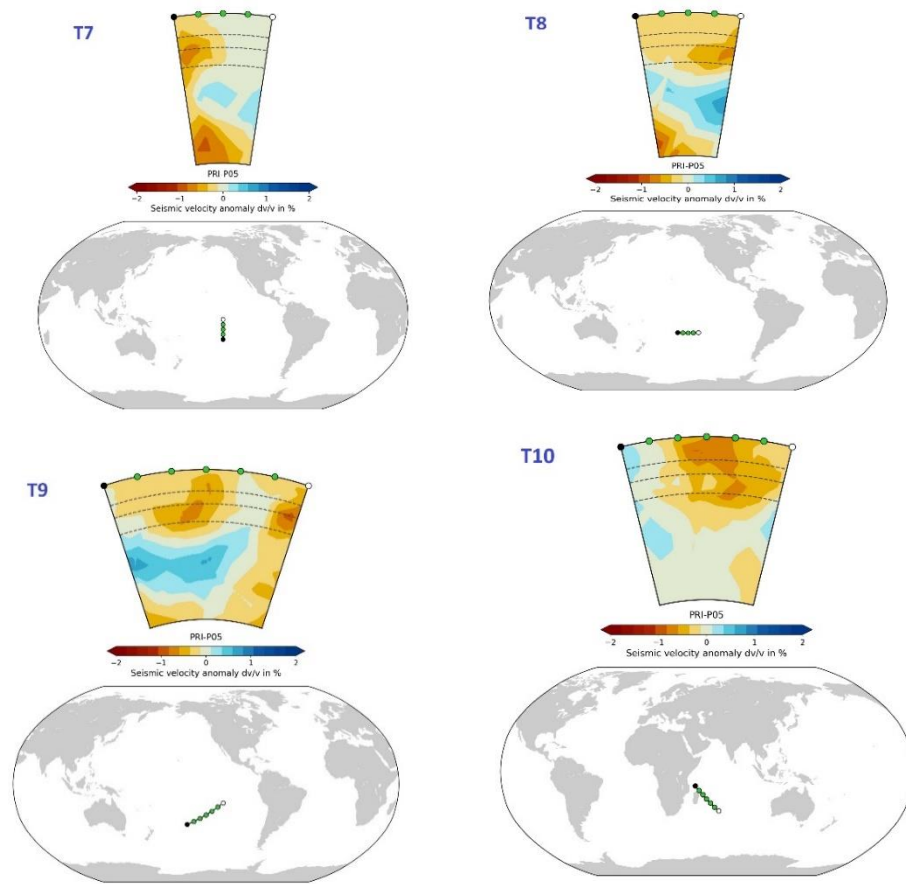
Fig 3.2: Tomographic sections under hotspot swells at: Afar (T1); Cobb (T2); Canary (T3); Galapagos (T4); Hawaii (T5); Iceland (T6); Marquesas (T7); McDonald (T8); Pitcairn (T9); Reunion (T10).

Table 3.1 (after Montelli et. al 2004)

Hotspot	Location	~ Depth (Km)	~ Radius (Km)
Afar (T1)	7 N, 39 E	1450	200
Canary (T3)	28 N,18 E	2800	400
Cobb (T2)	46 N, 130 W	1000	100
Galapagos (T4)	0 N, 92 W	1000	100
Hawaii (T5)	19 E, 155 W	2350	300
Iceland (T6)	64 N,17 W	1000	100
Reunion (T10)	21 S, 56 E	1900	200

Chapter 4

Physical modelling of Plume-lithosphere interactions

4.1 Theory of scaling

Often a thing is too large to be experimented with. Under such conditions, where mathematical analysis is not sufficient or where direct experimentation is needed, the best alternative is to study a study model. The geological problem of mountain building or of diastrophism is that they are not of the type that can be analyzed mathematically or experimented directly. The best alternative to study such phenomena is by means of experiments performed by building a proper scale model. Hundred years attempt have been made to perform studies of mechanism of rock deformation by such means. Hall, Daubree were some of the pioneer workers who built models to study the mechanism of folding and fractures.

 If the size of the body changes then other physical properties also change but is not proportional to the change of the size of the body. In order to investigate how various physical properties of a body changes with the change in size of a body, a cube of lead is considered. It is then enlarged n diameters and the density are kept constant. Let n be successively 1, 2, 3, 4, 5 and so on. Then it is investigated in what

manner the area, the volume, the mass, the weight and the pressure at the base of the cube change with different values of n.
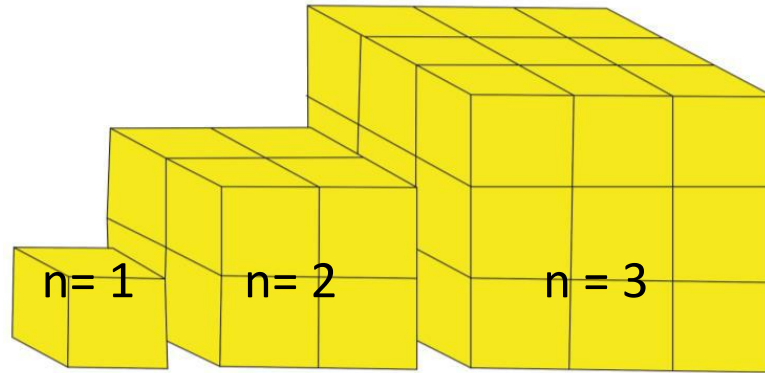

Fig. 4.1: Change of magnitude of a cube as the length of sides are changed (Hubbert, 1937)

When n=1, then each of the quantities are unity, that is, unit length, unit area, unit volume, unit mass, unit weight and unit pressure. When n=2, the length of the side=2, area=4, volume=8, mass=8, weight=8 and pressure at the base which is weight divided by area=2. When n=3, the length of the side=3, area=9, volume=27, mass=27, weight=27 and pressure at the base =3. The below table shows up to n=5.

Table 2.1: Change in physical properties with change in size of the body (Hubbert, 1937).

N	Length	Area	Volume	Mass	Weight	Pressure
1	1	1	1	1	1	1
2	2	4	8	8	8	2
3	3	9	27	27	27	3
4	4	16	64	64	64	4
5	5	25	125	125	125	5

From this it is understood that the area increases as square, the volume, mass, weight as cube and pressure at the base of the cube as the first power of the enlargement factor of a linear dimension of a cube, where gravity and density remain constant.

Geometrically Similarity: Two bodies are said to be geometrically similar when all corresponding lengths are proportional and all the corresponding angles in between two bodies are equal. If l1 be the length in one of the bodies and l2 be the corresponding length in other
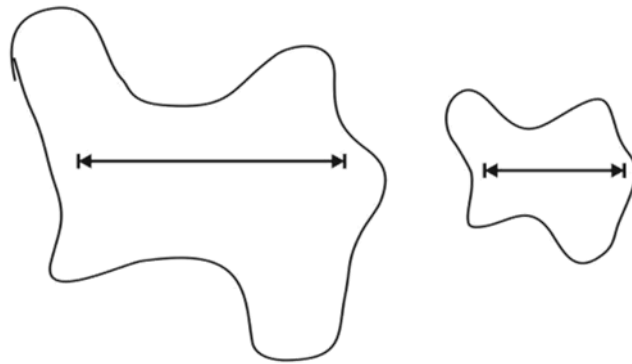

Figure 4.2: Two geometrically similar bodies (Hubbert, 1937)

$\frac{l1}{l2}$= λ, or l$_2$= λ l$_1$

where λ is constant of proportionality of length of the two bodies.

If the first body is considered to be original and the second body is replica of the first made to scale, then the second body is the scale model for the former one. If reduction occurs, then will be less than unity and if enlargement occurs then will be greater than unity. λ is the model ratio of length. λ is a familiar map scale extended to three dimensions.

In two geometrically similar bodies, the ratio of areas of the corresponding bodies will be equal to square of model ratio of length.

$$\frac{A2}{A1} = \lambda^2,$$

Where A2 and A1 are the corresponding areas of the two bodies respectively. If the two areas are divided into similar grid works of n squares each. Then,

$l2^2 / l1^2 = \lambda^2$

then for n such squares,

$A2 / A1 = n.\, l2^2 / n.\, l1^2 = \lambda^2$,

In two geometrically similar bodies, the ratio of corresponding volume for two bodies is,

$V2 / V1 = n.\, l2^3 / n.l1^3 = \lambda^3$,

Kinematic similarity: If two geometrically similar bodies undergo geometrically similar changes in shape and position, or both, then they are said to be kinematically similar provided the time for the given in one body is proportional to that required for the corresponding change in the second body.

$t2 / t1 = \tau$,

where t1 is the time required for the transformation to occur in the original body and t2 is the time required for the corresponding change in the model, and τ is the model ratio of time.

Similarity of velocity and acceleration: If two bodies are kinematically similar, then the velocities and accelerations of corresponding bodies must be proportional

$v2 / v1 = \eta = (l2/t2\,) / (l1 / t1\,) = \lambda / \tau = \lambda.\, \tau^{-1}$

where v1 and v2 are velocities of the corresponding bodies and is the model ratio of corresponding velocities.

For acceleration:

$a2 / a1 = \gamma = (l2 / t2^2) / (l1 / t1^2) = \lambda . \tau^{-2}$,

where γ is the model ratio of acceleration.

For angular velocities,

$\omega2 / \omega1 = (\theta2 / t2) / (\theta1 / t1) = (\theta2 / \theta1) . (t1 / t2)$,

where ω1 and ω2 are the angular velocities and θ1 and θ2 are the angles of rotation in the time t1 and t2 in the original and model respectively.

But, θ1= θ2

Therefore,

$\omega2 / \omega1 = 1 / \tau = \tau^{-1}$,

Dynamic similarity: While discussing the geometrical and kinematic similarity, the relation between forms and motion have been described and here mass is not considered. All the bodies contain mass. So the model needs to have mass distribution similar to that of the original one. If dm1 is the mass of an element of volume dv1, in the original and dv2 for corresponding element of volume, dv2, of the model such that the ratio is:

$dm2 / dm1 = \mu$,

And must hold for each point throughout the two bodies, μ being the model ratio of mass. From model ratio of mass and length, the ratio of density can be obtained.

The density can be defined by mass divided by volume. Model ratio of density δ is given by,

$$\delta = \rho 1 \,/\, \rho 2 = (dm2 \,/\, dv2) \,/\, (dm1 \,/\, dv1) = \mu \; . \; \lambda^{-3},$$

and is a constant throughout the two bodies.

4.2   Experimental set up

The physical interaction was studied in a two layer model where the mantle is represented by water and the lithosphere by PDMS material in a glass tank of dimensions 60cmx30cmx30cm. Water is a low viscosity, high density and Newtonian fluid. While PDMS (Poly Dimethyl Siloxane) is a high viscosity, low density is a viscoelastic material that behaves in a quasi-Newtonian manner, if strain rates are low enough to neglect its elastic component, as is the case in this experiment (Weijermars and Schmeling, 1986; Funiciello et al., 2003). The mantle plume is produced by the low density PDMS rising through water from the bottom of the glass tank. The viscosity of the plume is higher unlike the natural case. This helps to keep the volume of the plume head volume intact and prevent the head from mixing. The experiments are carried in natural condition so that none of the physical parameters change with temperature. Thermal effects and phase changes are neglected, and the dynamics of the whole system is controlled by the interplay between compositional buoyancy and viscous forces.

 For our experiments, we first place a wooden plank of dimension 55cmx15cmx1cm containing a circular groove of 12.5 cm circular radius and depth 1cm. The dyed PDMS was poured into the groove. The plank was then placed into the bottom of tank, filled with water upto a height of 17cm. It is ensured that the grove lies almost in the middle of the tank. After positioning the "lithospheric plate" of dimension

25cmx10x05.cm on the surface of water, the system is left to reach an isostatic, steady state conditions. The lithosphere is not attached and is free to rotate on the surface of water without any hindrance. Since source material has a lower density compared to water, Rayleigh-Taylor instability builds up and plume rises through the water, the ascent is recorded in a front view camera. Perspective 3D view is recorded with a camera from the side. To understand the rate of lateral flow, a top view camera is fixed to the top of the tank to record the change.
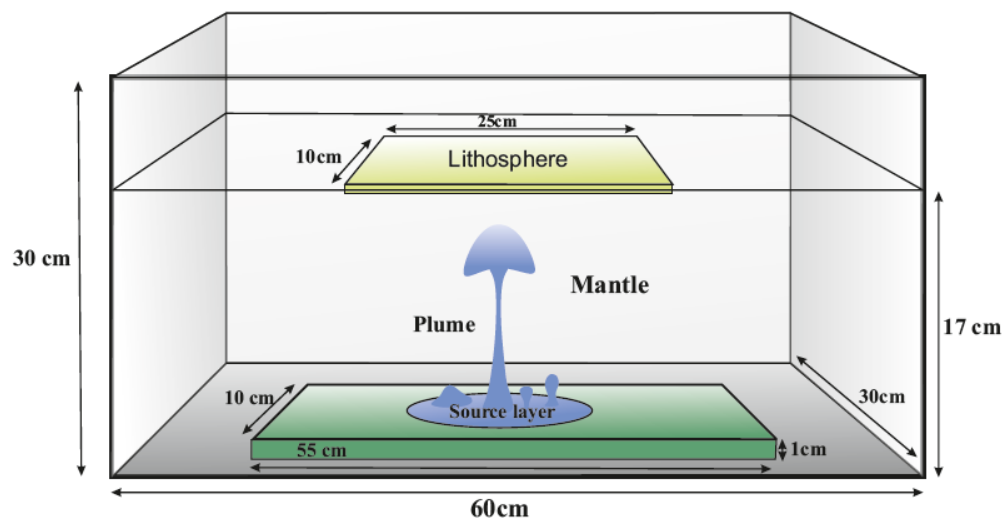

Fig. 4.3: Laboratory experimental setup in schematic diagram.

4.3   Model materials and physical variables

The plume is modeled using transparent Polydimethylsiloxane (PDMS). It belongs to a group of polymeric organo-silicon compounds known as silicones. It has unusual rheological (or flow) properties. PDMS is viscoelastic. At long flow times (or high temperatures), it behaves as a viscous liquid similar to honey. But at short

flow times (or low temperatures), it behaves as an elastic solid similar to that of rubber. Is some PDMS is left overnight in a container; it will flow to cover the surface and mold to the surface of the container. However if the same PDMS is rolled into a sphere and thrown in to the surface (short flow time), it will bounce back like a rubber ball. The solid PDMS samples have external hydrophobic surface which prevent polar solvents like water to wet the surface of PDMS which appears shiny and metallic. In experiment two kind of PDMS is used as plume material, one with a higher viscosity (55Pa-s) and other with a lower viscosity (50Pa-s). The PDMS used as lithosphere has highest viscosity of range 5×10^4 Pa-s.

Water used is clean and without any contamination. Water is a Newtonian fluid with higher density compared to PDMS. Viscosity of water is also less compared to the PDMS.

Table 4.1: Material properties

Layer	Material	Density	Viscosity
Lithosphere	PDMS	965 Kg/m3	5 x 10 ^ 4 Pa-s
Mantle	Water	1000 Kg/m3	9 x 10 ^ -3 Pa-s
Plume	Low viscosity PDMS	800 Kg/m3	50-55 Pa-s

4.4   Experimental findings and observations

The objective of the experiment is to study the interaction of plume with lithosphere under different dynamic conditions. For that we choose two source materials with different viscosities.

Experiment 1: A low viscosity PDMS (50 Pa-s) of volume 50 cc is taken as source layer material in the grove. The water level is taken to be 17 cm. The lithosphere thickness is 0.5cm. The source material being lower density compared to water develops perturbations on the surface of source layer after 30 minutes, when the system was left undisturbed. These are Rayleigh-Taylor instability formed on the surface of low density material when overlain by high density material. The dynamics of the ascent of the source material is recorded subsequently with progress of time (t) from the onset of R-T instability generation. (Fig. 4.4) After t=3 min, a vertical channel of rising source material is produced. The rising plume has a bulbous head with a thin slender tail that remains connected to the source layer. The plume rises through the water column initially with a low velocity of 0.85cm/min. Then the velocity increase to 2.83 cm/min as it reaches near the base of lithosphere when t=12.5 min (Fig 4.4). As the plume head reaches the base, it imparts a torque on the lithospheric plate and the plate rotates. The plume head material accumulates below the lithosphere as plume under-plating. As the entire volume of material in the plume head stagnates, a continuous supply of material from the source layer is maintained through the stem (Fig 4.5). So the volume of plume material accumulating at the base of the lithosphere increases with time until the stem is completely detached from the source layer. A surface topography is formed on the lithospheric plate with continuous stagnation of buoyant plume material at the base. The material begins to flow laterally under the plate. However, the rate of spread of viscous plume material is very slow and is not uniform in all directions.

Experiment 2: The source material is changed to a higher viscosity PDMS (55 Pa-s) of volume 120cc is taken. The water level is 17cms and the dimensions of

lithosphere are kept same as in the previous experiment. After 40 min of initiation of experiment, the R-T instability develops in the source layer at t =0 min. A conduit of plume material starts to rise through the mantle at t = 5min. The dynamics of the plume is however different from the previous experiment. A bulbous head is trailed by successive pulses of source material rising through the tail (Fig 4.6). The plume head hits the base of lithosphere at t= 30 min and rotates the plate (Fig 4.6). As the plate rotates on the surface of the water, the material stagnates as a trail. Maximum volume of head material accumulates at a point where plume hits the base initially forming blobs. Successive pulses form voluminous accumulation at certain intervals in the trail (Fig 4.7). A sharp surface topography is produced at the surface as the plume material accumulates (Fig 4.8).

4.5   Results

The plume dynamics is dependent on the physical parameters of the plume. When a low viscosity material is used (50 pa-s), it shows a *continuous plume dynamics* with a bulbous head and narrow slender tail connected to the source layer. A continuous supply of material is maintained by the plume tail, until the tail breaks off. With increase in viscosity of the plume material (55 Pa-s), the regime changes to a *pulsating plume dynamics*. In case of continuous plume dynamics, stagnation of plume material happens at the point of impact of plume head under lithosphere. However under pulsating dynamics material accumulation happens along a trail, with voluminous accumulations formed when successive smaller pulses of source material hits the lithosphere. The lateral flow of material is slow at the base of lithosphere owing to high viscosity contrast between the lithosphere and plume

material. Thus, the physical investigations reveal that the dynamics as well as the stagnation pattern depends on the viscosity of the plume material. Both the dynamics show formation of surface topography due to stagnation.
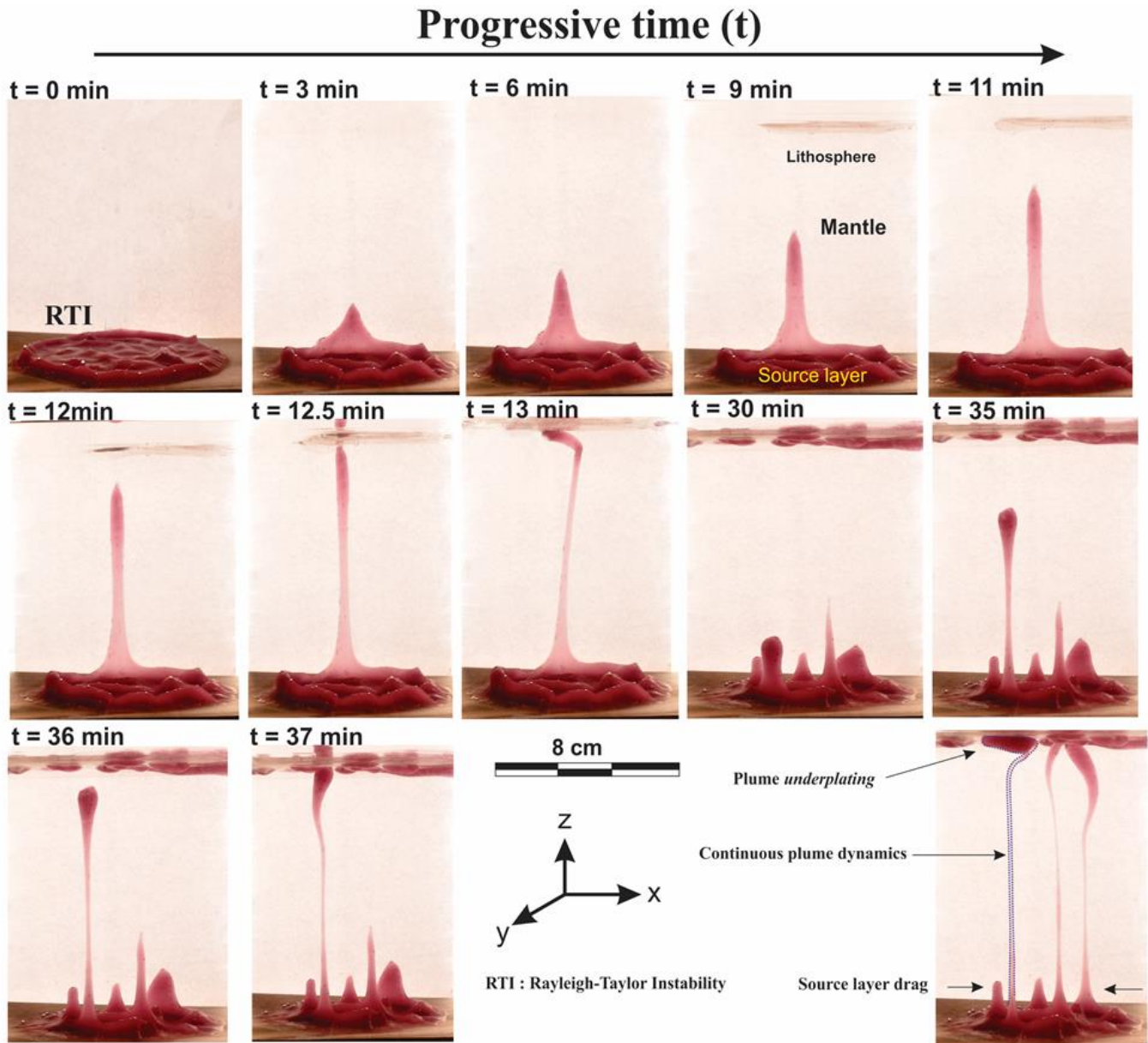

Fig 4.4: Continuous plume ascent through progressive time in Experiment 1, showing the formation of RTI and generation of plumes that stagnate at the point of impact. Here the viscosity of plume is 50 Pa-s.
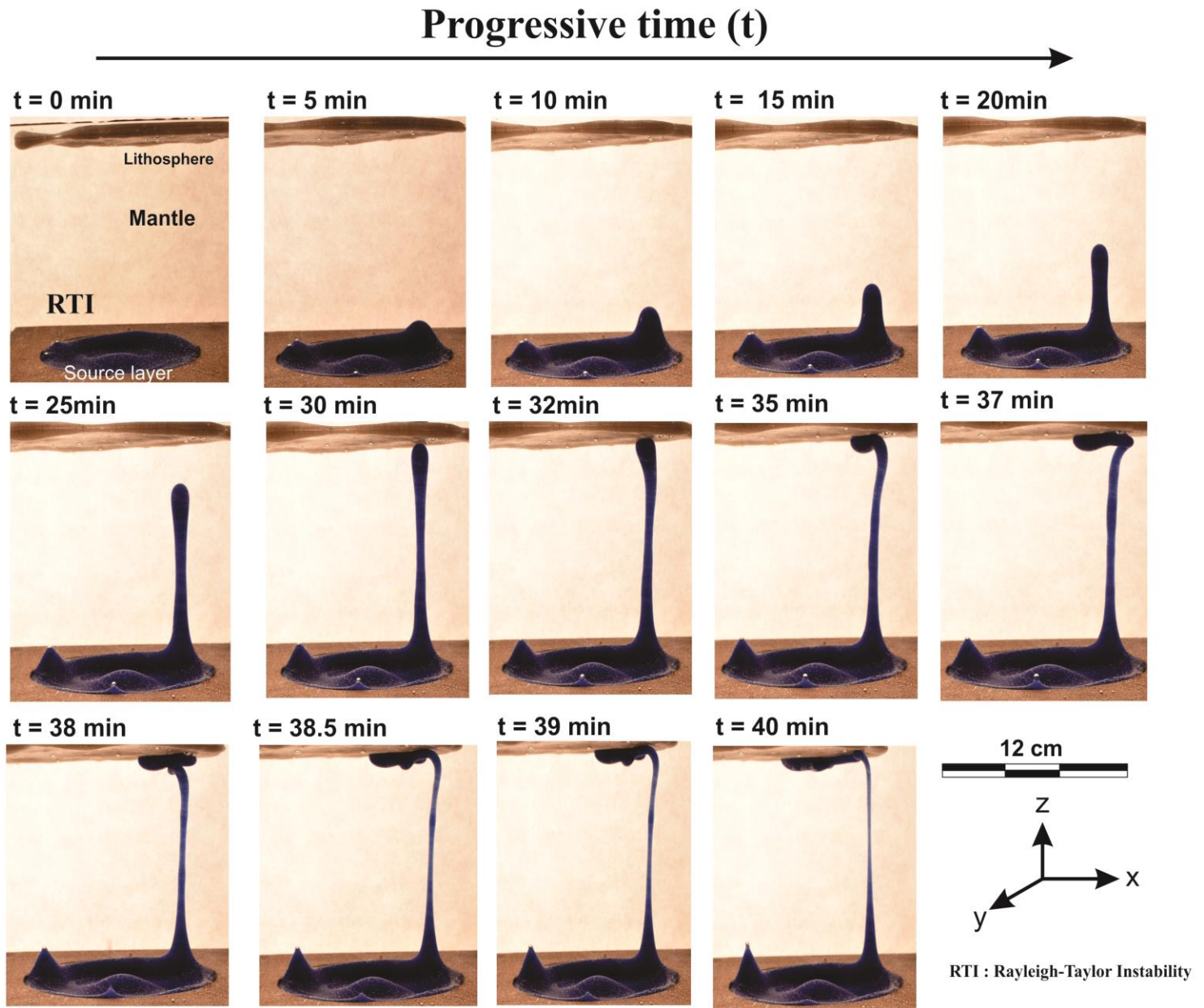
Progressive time (t)

Fig 4.5: Pulsating plume ascent through progressive time in Experiment 2, where stagnation happens in voluminous pulses under lithosphere. Here the viscosity of plume material is 55 Pa-s
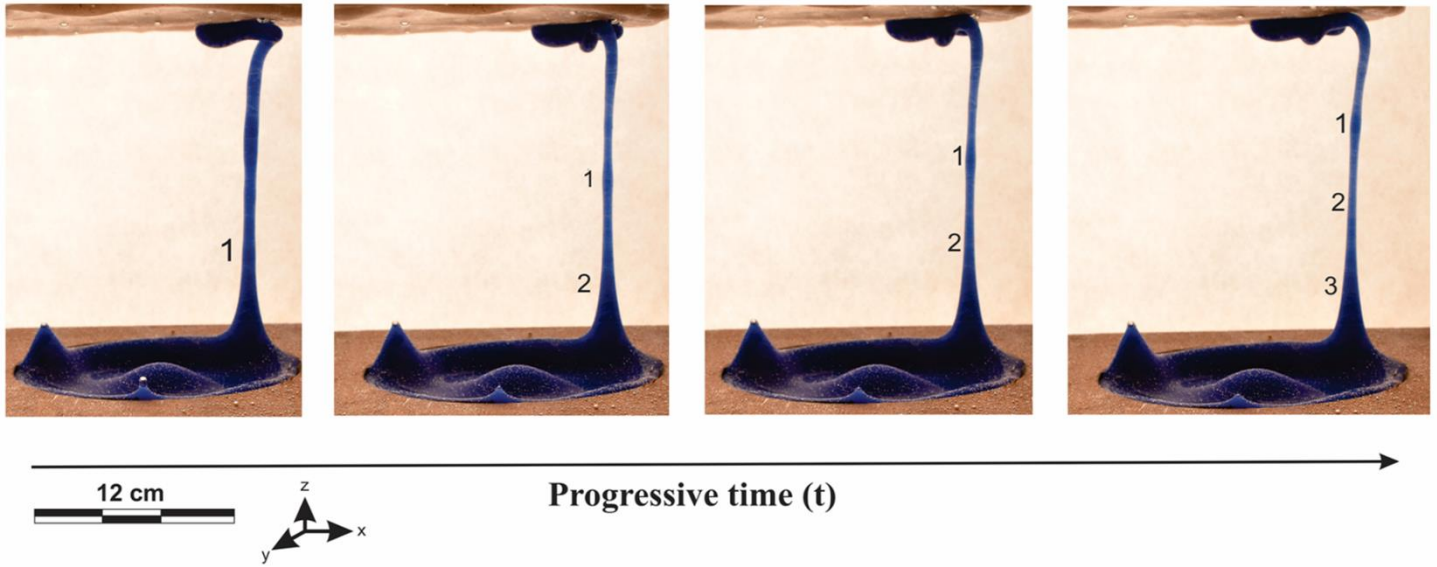
Pulsating dynamics

12 cm

Progressive time (t)

Fig 4.6: Pulses of plumes (1,2,3) rising through mantle in Experiment 2, with high viscosity plumes.

Blobs of plume material under lithosphere
i.e. *plume underplating*

Final topography in the lithosphere

2 cm
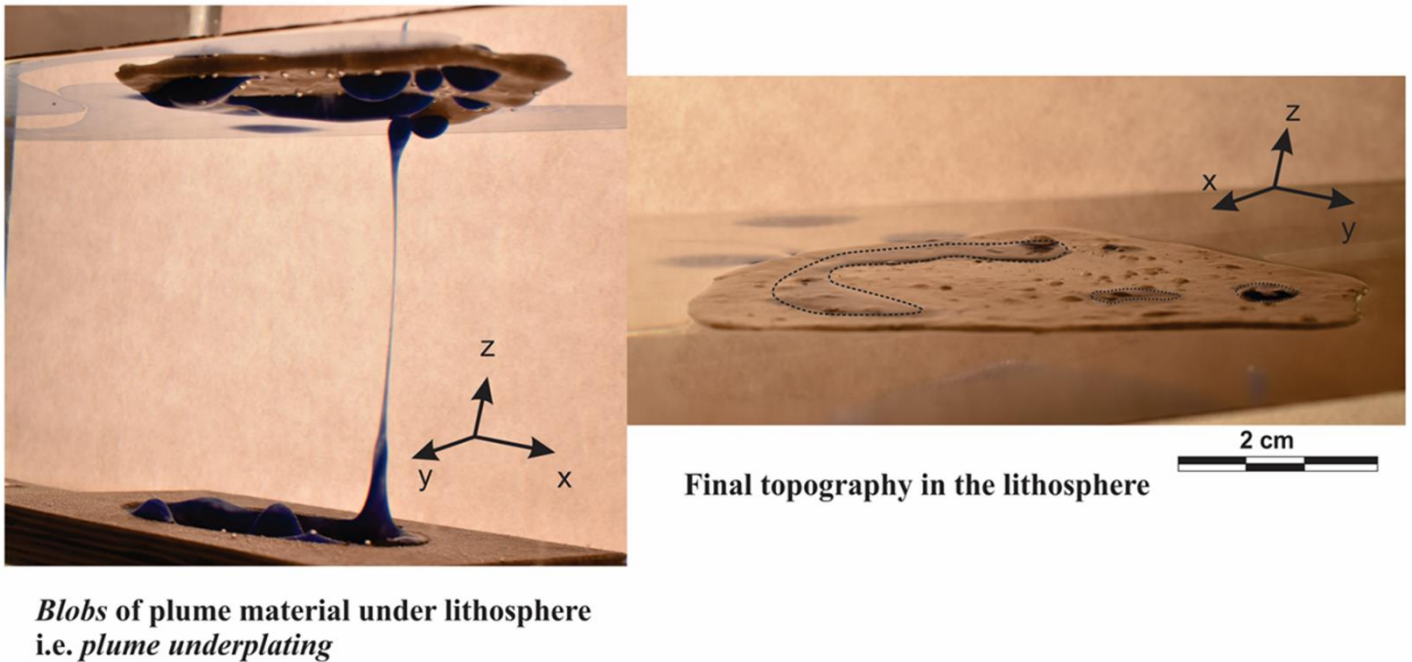
Fig 4.7: Plume stagnation at the base of lithosphere and the corresponding surface topography generated in Experiment 2.
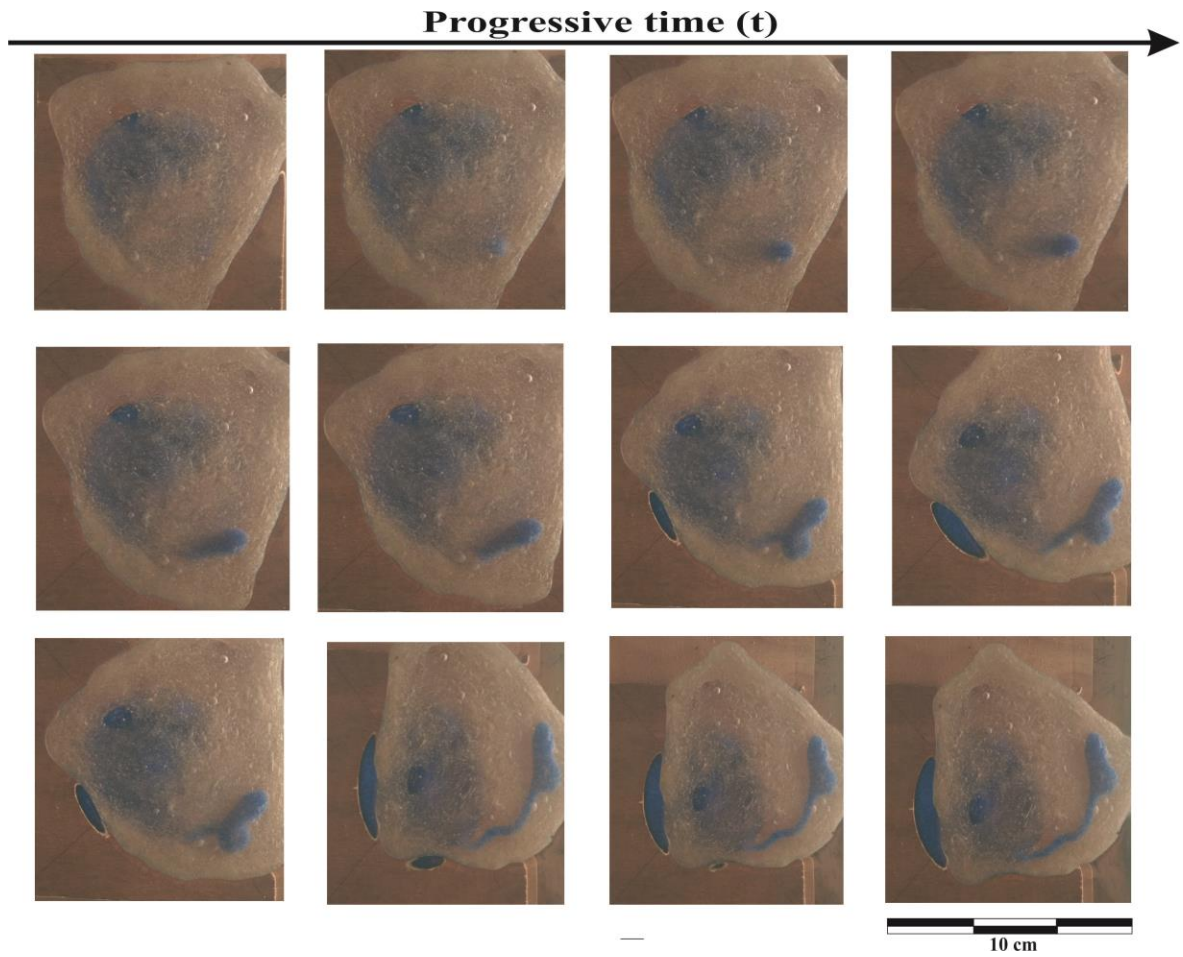
10 cm

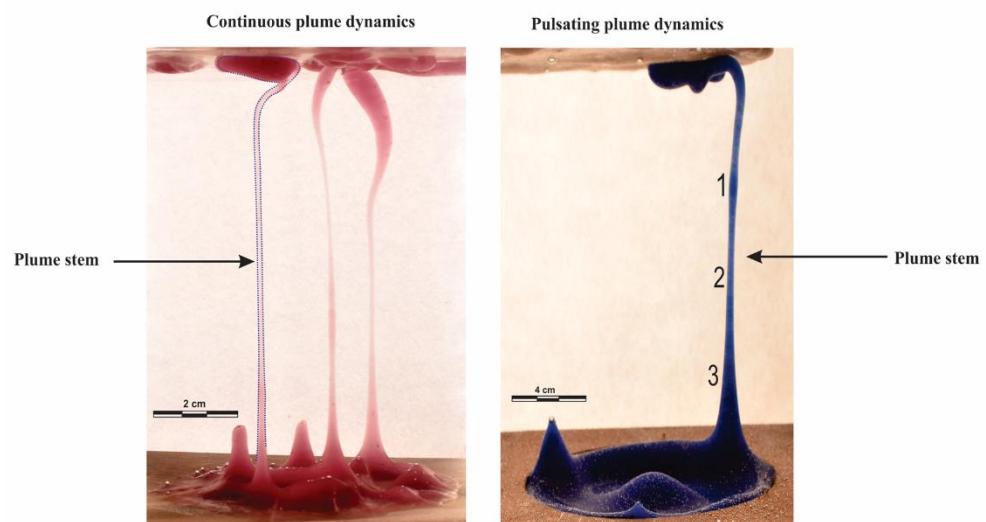Fig 4.8: Trails of plume stagnation at the base of lithosphere in Experiment 2, (top view)

Fig 4.9: Continuous vs pulsating plume dynamics

Chapter 5

Plume-lithosphere interactions from finite element (FEM) modelling

5.1 Physics of ASPECT

To verify our experimental model we performed numerical simulations in ASPECT (Advanced Solver for Problems in Earth's ConvecTion). It is a massively parallel finite element code characterized by modern numerical methods, parallelism and extensibility via plug-ins. It was originally designed for modeling thermal convection in the mantle. The code is based on state-of-the-art numerical method such as adaptive mesh refinement (AMR), accurate discretizations, efficient linear and iterative solvers and parallelization. ASPECT consists of a small core which solves the basic equations. For other tasks it relies on external libraries and plug-ins (Fraters, 2014, Kronbichler et al., 2012). The DEAL.II software library (Bangerth et al., 2007) supports the creation of finite element codes. Which, in turn, depends on p4est (Burstedde et al., 2011) for adaptive mesh refinement and parallelization and on TRILINOS (Heroux, 2005) for solvers to solve the linear and non-linear systems of equations and all of them are in constant development.

5.1.1 Basic equations

Like other geodynamics codes ASPECT assumes that the solid Earth materials can be treated as a highly viscous fluid and hence the Stokes equation can be solved. It solves a system of equations driven by differences in the gravitational force due to a density that depends on the temperature. Specifically, we consider the conservation of momentum, mass and energy.

$$-\nabla \cdot \left[2\eta \left(\varepsilon(\mathbf{u}) - \frac{1}{3}(\nabla \cdot \mathbf{u})\mathbf{1} \right) \right] + \nabla p = \rho \mathbf{g} \qquad \text{in } \Omega, \qquad (1)$$

$$\nabla \cdot (\rho \mathbf{u}) = 0 \qquad \text{in } \Omega, \qquad (2)$$

$$\rho C_p \left(\frac{\partial T}{\partial t} + \mathbf{u} \cdot \nabla T \right) - \nabla \cdot k \nabla T = \rho H$$

$$+ 2\eta \left(\varepsilon(\mathbf{u}) - \frac{1}{3}(\nabla \cdot \mathbf{u})\mathbf{1} \right) : \left(\varepsilon(\mathbf{u}) - \frac{1}{3}(\nabla \cdot \mathbf{u})\mathbf{1} \right) \qquad (3)$$

$$+ \alpha T (\mathbf{u} \cdot \nabla p)$$

$$+ \rho T \Delta S \left(\frac{\partial X}{\partial t} + \mathbf{u} \cdot \nabla X \right) \qquad \text{in } \Omega,$$

$$\frac{\partial c_i}{\partial t} + \mathbf{u} \cdot \nabla c_i = q_i \qquad \text{in } \Omega, i = 1 \ldots C$$

$$(4)$$

where $\varepsilon(\mathbf{u}) = \frac{1}{2}(\nabla \mathbf{u} + \nabla \mathbf{u}^T)$ is the symmetric gradient of the velocity (often called the *strain rate*).[1]

In this set of equations, (1) and (2) represent the compressible Stokes equations in which $\mathbf{u} = \mathbf{u}(\mathbf{x}, t)$ is the velocity field and $p = p(\mathbf{x}, t)$ the pressure field. Coupled to this Stokes system is equation (3) for the temperature field $T = T(\mathbf{x}, t)$ that contains heat conduction terms as well as advection with the flow velocity $\mathbf{u}$. The right-hand side terms of this equation correspond to internal heat production for example due to radioactive decay, friction heating, adiabatic compression of material and latent heat due to phase change. Equation (4) represents the advection of the compositional fields.

5.1.2 Time discretization

The size of the chosen timestep is very important in numerical geodynamics as if the timesteps are large, the solver may not be able to find a good solution, whereas if the timesteps are too small, a lot of computational time will be needed to get the desired result. To solve this problem Courant-Friedrich-Lewy (CFL) condition is introduced. The time step k is chosen according to

$$k = c \min_K \frac{h_K}{\|u\|_{\infty,K} p_T} \qquad (5)$$

Where h_K is the diameter of cell K, and the denominator is the maximal magnitude of the velocity on cell K times the polynomial degree p_T of the temperature discretization. The dimensionless constant c is called the CFL number in this program.

5.1.3 Solving the equations

In FEM the discretized basis equations are written in a matrix-vector form. The set of linear equations in its simplest form looks like

$$A\,x = b \qquad (6)$$

Where A is a $n \times n$ matrix, and x and b are vectors of length n, where n is the number of unknowns. Vector b contains the boundary conditions and buoyancy forces. Vector x contains the unknowns of the system to be solved, such as velocity, pressure temperature.

Here we used an iterative solver to solve our basic matrix-vector equation. Although it doesn't solve the equation immediately, it requires much less memory

than a direct solver and hence computationally much less expensive. Iterative solvers use the previous solution of vector **x** as a starting condition to solve the system of equations again. ASPECT calculates the linear residual vector **r** of the system (the *inner iteration*) defined by

$$r = Ax - b \qquad (7)$$

for each iteration and when the *L*2 norm of vector **r** is smaller than a user defined tolerance, the system is seen as solved. Then it moves from *inner iteration* to the *outer iteration*.

Within *outer iteration*, first the strain-rate is recomputed and based on the strain-rate, the viscosity is recomputed. If the relative residual

$$\left(\frac{\|R_n\|_2}{\|R_0\|_2} \right)$$

is not smaller than a user defined value, matrix **A** is updated as it is dependent on strain-rate and viscosity. With this new **A**, the system is solved again. When the nonlinear iterations have converged, the velocity field is used for advection of the material. The complete algorithm is shown in (Fig. 5.1)
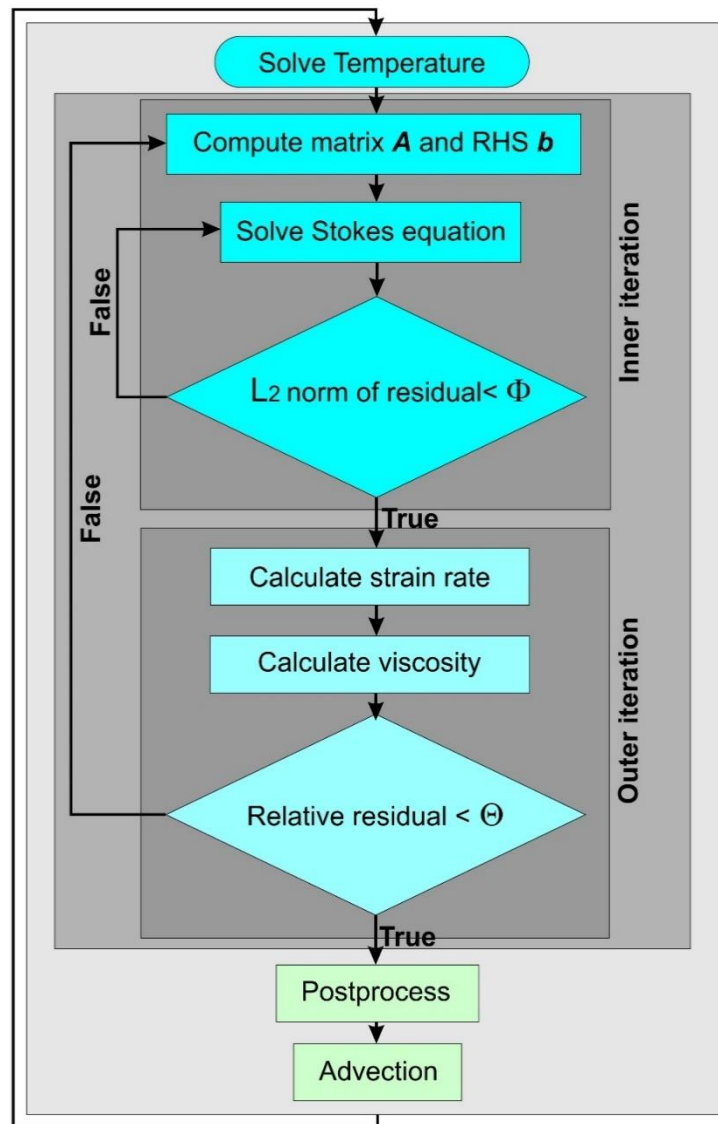
Fig 5.1: Algorithm for computation in each time step in ASPECT

5.1.4 Rheology

Our simulations adopt a visco-plastic rheology for earth materials. The plastic behavior is modeled here for rocks at a relatively low temperature condition. Plastic yielding is implemented by locally rescaling the effective viscosity in such a

way that if stress exceeds the yield stress, the viscosity is rescaled back to the yield surface. The effective plastic viscosity is thus given by

$$\mu_{\text{eff}}^{\text{pl}} = \frac{\sigma_y}{2\dot{\epsilon}_{\text{e}}},\qquad(8)$$

σy being yield value. Plasticity limits viscous stress through a Drucker Prager yield criterion, where the yield stress in 2D is

$$\sigma_y = C\cos(\phi) + \sin(\phi)P,\qquad(9)$$

C is cohesion and φ is the angle of internal friction. Note that the 2D form is equivalent to the Mohr Coulomb yield surface. If φ is 0, the yield stress is fixed and equal to the cohesion (Von Mises yield criterion).

At higher temperature, rocks experience nonlinear viscous deformation, expressed by a temperature and strain rate dependent viscosity. There are two deformation mechanisms commonly associated with a viscous rheology (fig5.2):

• *Dislocation creep:* Deformation through this mechanism is caused by deformation of the crystals in the material. This process can be activated at low stresses, and is very stress dependent but not dependent on grain-size.

• *Diffusion creep:* Deformation through this mechanism works through the movement of vacancies, i.e. the filling of vacancies which causes the opening of new vacancies, through the material. This process is linearly dependent on stress and strongly dependent on grain-size.

The viscosity for dislocation or diffusion creep is defined as:

$$v = \frac{1}{2} A^{-\frac{1}{n}} d^{\frac{m}{n}} \dot{\varepsilon}_{ii}^{\frac{1-n}{n}} \exp\left(\frac{E + PV}{nRT}\right)$$ (10)

where A is the prefactor, n is the stress exponent, $\dot{\varepsilon}_{ii}$ is the square root of the deviatoric strain rate tensor second invariant, d is grain size, m is the grain size exponent, E is activation energy, V is activation volume, P is pressure, R is the gas exponent and T is temperature. For diffusion creep μ^{df}; $n = 1$, $m! = 0$ and for dislocation creep μ^{dl}, $n > 1$, $m = 0$.

Both types of viscous creep act simultaneously under the same deviatoric stress, so the contributions of diffusion μ^{df} and dislocation μ^{dl} creep to the effective viscosity are harmonically averaged into a composite viscosity

$$\mu_{eff}^{cp} = \left(\frac{1}{\mu_{eff}^{df}} + \frac{1}{\mu_{eff}^{dl}}\right)^{-1}.$$ (11)

To combine plastic yielding and viscous creep, we assume a harmonic averaging scheme

$$\mu_{eff}^{vp} = \left(\frac{1}{\mu_{eff}^{cp}} + \frac{1}{\mu_{eff}^{pl}}\right)^{-1} = \left(\frac{1}{\mu_{eff}^{df}} + \frac{1}{\mu_{eff}^{dl}} + \frac{1}{\mu_{eff}^{pl}}\right)^{-1}.$$ (12)
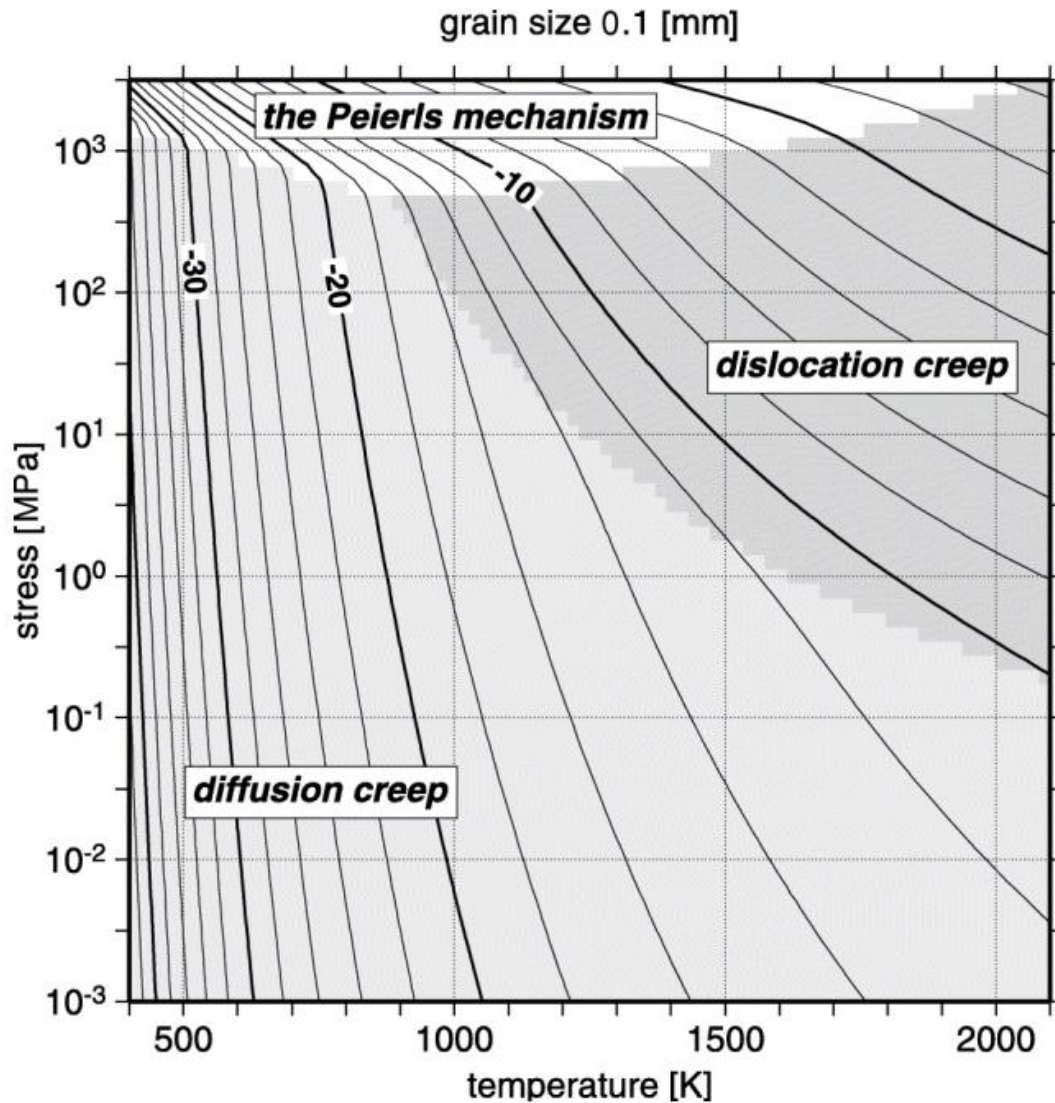
Fig 5.2: Different micro-deformation regimes as function of stress, grain size and temperature

5.1.5 Free surface calculations

The upper surface is considered as free surface in order to observe the change in elevation with time. For this we require zero stress on this surface. Since there will be flow across the surface we also need to have a dynamically deformable mesh. To handle the motion of the mesh with a free surface ASPECT incorporates the

arbitrary Lagrangian-Eulerian (ALE) implementation. The ALE approach allows the mesh motion $\mathbf{u}_m$ to be largely independent of the fluid. The mass conservation condition requires that $\mathbf{u}_m \cdot \mathbf{n} = \mathbf{u} \cdot \mathbf{n}$ on the free surface, but otherwise the mesh motion is unconstrained, and should be chosen to keep the mesh as well behaved as possible. The mesh velocity is calculated by using a Laplacian scheme given by

$$
\begin{aligned}
-\Delta \mathbf{u}_m &= 0 && \text{in } \Omega, \\
\mathbf{u}_m &= (\mathbf{u} \cdot \mathbf{n})\,\mathbf{n} && \text{on } \partial\Omega_{\text{free surface}}, \\
\mathbf{u}_m \cdot \mathbf{n} &= 0 && \text{on } \partial\Omega_{\text{free slip}}, \\
\mathbf{u}_m &= 0 && \text{on } \partial\Omega_{\text{Dirichlet}}.
\end{aligned}
$$

(13)

After calculating mesh velocity, mesh vertices are time-stepped explicitly for minimally distorting perturbation to the mesh. To further stabilize the free surface, a quasi-implicit free surface integration scheme (Kous 2010) is incorporated.

5.2 Model geometry

All the models have a 2D Cartesian geometry with horizontal distance of 1000 km and a model height of 440 km, except for the special case where upper surface is a free surface (sticky air is removed) in which case the model has a height of 410 km. The model height is divided into 7 horizontal compositional fields. The first layer is sticky air and has a thickness of 30 km. Next compositional field is the crust which is divided into upper crust with a thickness of 25 km and a lower crust with a thickness of 15 km. The following compositional field is the lithospheric mantle whose thickness varies from 40-80 km. The rest of the model depth is made up of

upper mantle. A semicircular plume is introduced at the base of the model with a radius that varies from 20-100 km. In addition, a rectangular seed (present due to pre-rift tectonic history) is incorporated at the boundary between lower crust and lithospheric mantle. The model geometry is shown in Fig. 5.3 and the properties are listed in Table (5.1).
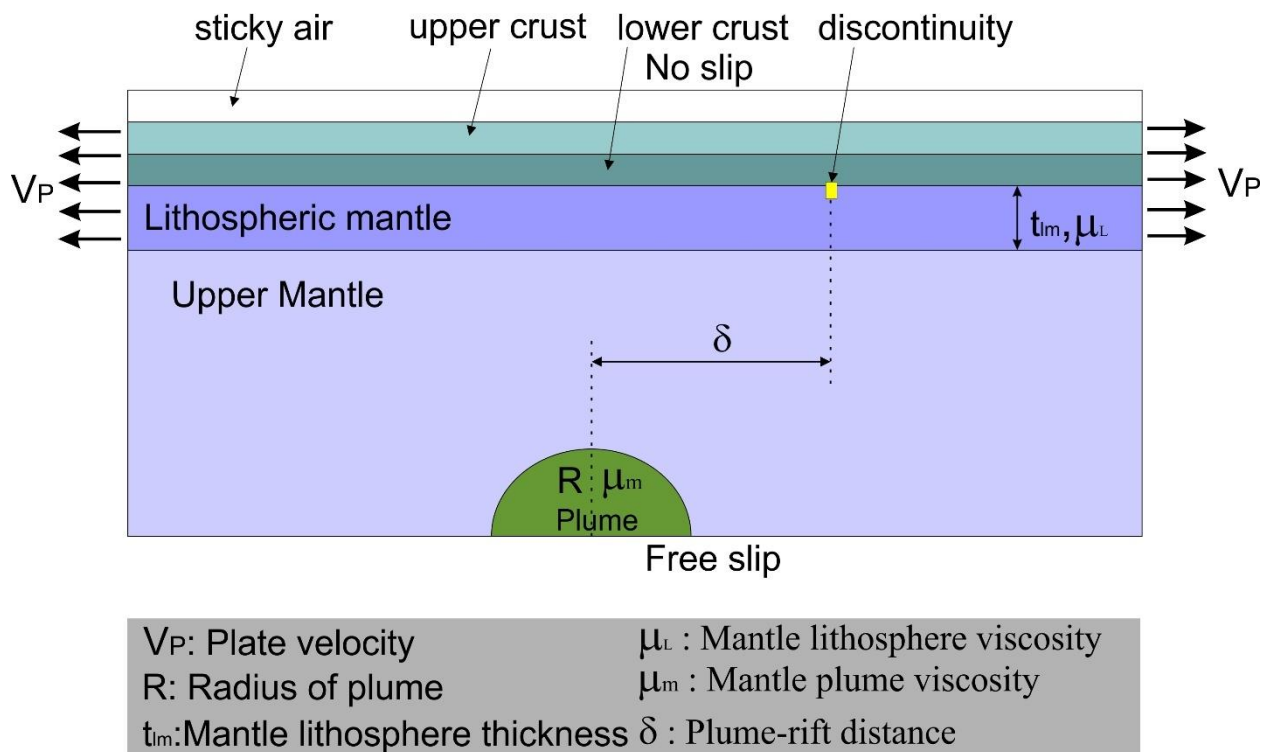

Fig. 5.3: Model geometry in ASPECT

Parameters	Values
Model length(L)	1000km
Model height(H)	410km
Thickness- upper crust(t_{uc})	25km
lower crust(t_{lc})	15km
lithospheric mantle(t_{lm})	40-80km
Plume diameter	20-100km
Plate velocity	0.25-5cm/year
Plume-rift distance	0-300km
Surface Temperature (Ts1)	293 K
Temperature at upper crustal base (Ts2)	681 K
Temperature at lower crustal base (Ts3)	823 K
Temperature at the base of the lithosphere (Ts4)	1573 K
Model base temperature (Tb)	1700 K
Initial plume temperature (Tp)	1700-1900 K
Heat production at upper crust (A)	1.5e-6 W/m^3
Thermal conductivity- upper crust (k1)	2.5 W/m.K
lower crust (k2)	2.5 W/m.K
lithospheric mantle (k3)	3.5 W/m.K
Layer surface heat flow- upper crust (qs1)	0.065357 W/m^2
	0.035357 W/m^2
lower crust (qs2)	0.035357 W/m^2
lithospheric mantle (qs3)	

Table 5.1: Model parameters properties

5.2.1 Discretization of the domain

In order to solve a model problem in ASPECT (on any other FEM based code), the domain has to be discretized. Our domain is discretized into quadrilateral finite elements. Basis functions are then defined for the independent variables such as velocity, pressure, temperature and compositional fields. Here we employ second-order polynomials for velocity, and first-order polynomials for pressure (Q_2Q_1 elements), and also second order polynomials for temperature and composition. We have always used square grid to solve our problem where all the cells have the same height and width. The model domain is subdivided in such a way that it has a

finite element grid with uniform 2 km spacing. Adaptive mesh refinement (AMR) is turned off in all the models in order to avoid numerical errors.

5.2.2 Formulation and CFL number

Here we choose a custom formulation which is equivalent to extended Boussinesq approximation. The compressibility of the model is chosen from the material model which returns an incompressible Stokes approximation given by

$$
\begin{aligned}
-\nabla \cdot [2\eta\varepsilon(\mathbf{u})] + \nabla p' &= -\bar{\alpha}\bar{\rho}T'\mathbf{g} && \text{in } \Omega, \\
\nabla \cdot \mathbf{u} &= 0 && \text{in } \Omega.
\end{aligned}
$$
(14)

Combining Eq. (14) and Eq. (4) allows the shear-heating and adiabatic term to be dropped from the energy equation. But the extended Boussinesq approximation brings back the shear-heating term and the adiabatic heating term into the equation.

For our cases we varied the CFL number from 0.1 to 0.5.

5.2.3 Initial condition

Initial temperature: The initial temperature profile is adiabatic with a potential temperature of 1600 K.

This adiabatic profile is superimposed with a conductive temperature profile for the continental lithosphere. If the layer has thickness dz, then the temperature at, and heat flow through, the bottom of the layer (T_B, q_B) can be expressed in terms of the temperature and heat flow at the top of the layer (T_r, q_r) and properties (A,k) of the layer

$$T_B = T_T + \frac{q_T}{k}\Delta z - \frac{A\,\Delta z^2}{2k} \qquad (15)$$

$$q_B = q_T - A\,\Delta z \qquad (16)$$

Equations (15) and (16) are applied to successive layers, resetting T_T and q_T at the top of each new layer with the values T_B and q_B solved for the bottom of the previous layer. The temperature profile is shown in (fig.5.4). A temperature perturbation of 200 K is added to the plume material at of the bottom boundary of the model.
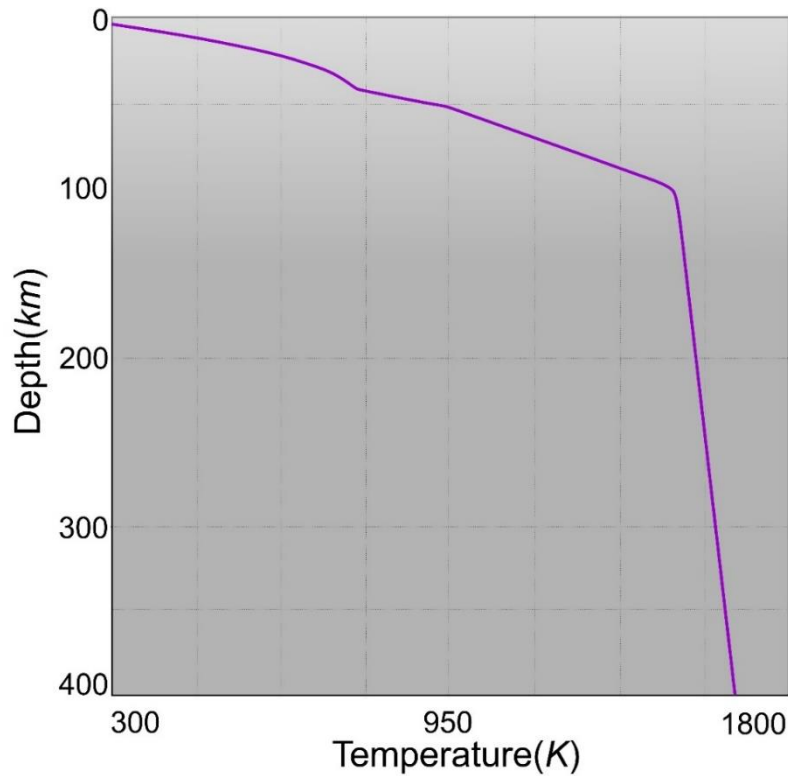
Fig 5.4: Distribution of temperature with depth

Initial density: The density is primarily dependent on the composition but in a compressible medium it depends also on pressure, and temperature whereas in an incompressible medium it depends only on temperature. The density depends on pressure and temperature via the following two equations:

$$\rho_{incomp} = \rho_{ref}(1.0 - \alpha(T - T_{ref}))$$

$$\rho_{comp} = \rho_{ref}(\beta(P - P_{surface}))(1.0 - \alpha(T - T_{ref})) \qquad (17)$$
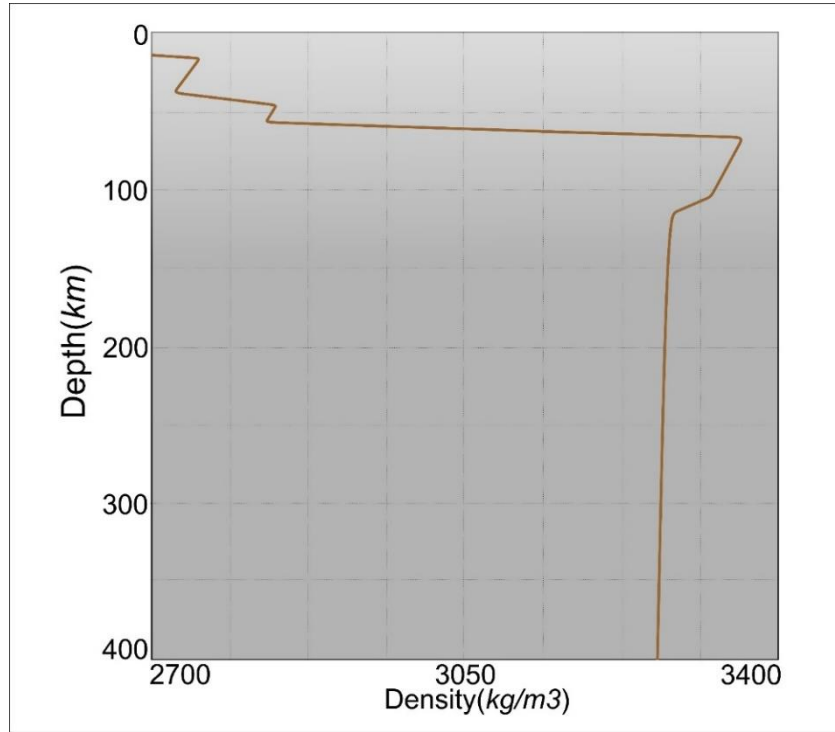
Fig 5.5: Density distribution vs. Depth

Since our visco-plastic model is incompressible in nature, the density variation will follow eq (8). The variation of density with depth is shown in fig. (5.5).

Initial viscosity

A viscosity profile is also needed to properly model the interaction of plume and lithosphere. Our viscosity profile is referenced from Cızkova et al. (2012) who

determined the viscosity profile from the inferred sinking speed of remnants of subducted lithosphere in the mantle and from Blom (2016) whose viscosity profile is located under a static continental crust where stresses are low.

The viscosity is calculated in ASPECT using flow laws given in equation (2). They are dependent on pressure, temperature, strain rate. Our profile has a high viscosity upper crust followed by a relatively low viscosity lower crust, which follows a lithospheric mantle whose viscosity gradually decreases from high (equivalent to upper crust) to moderate due to increase in temperature. This is followed by upper mantle which has even lower viscosity. The viscosity profile of our model as well as the other two models are shown in fig. (5.6).
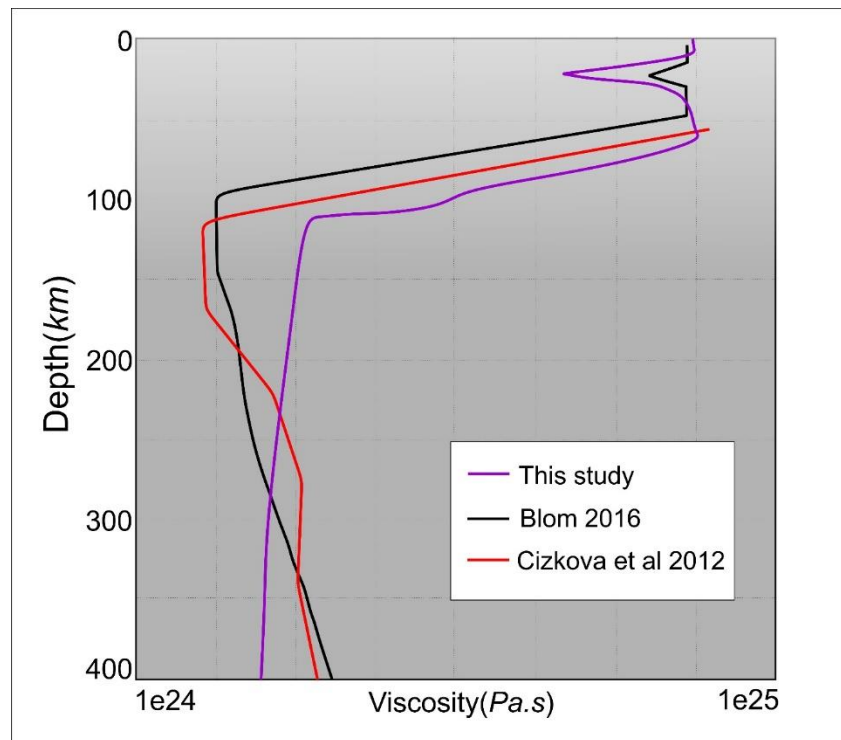
Fig. 5.6: Viscosity vs Depth

5.2.4 Boundary condition

The boundary composition and temperature is the same as the initial composition and temperature. The bottom boundary is *free slip* and *isothermal* with a maximum temperature of 1700 K. The top boundary is *free surface* (or *free slip*) and *isothermal* with a minimum temperature of 293 K (or 273 K) (Table 5.1). The side boundaries are *insulating* in nature. A prescribed diverging velocity profile of 0.25 cm/year to 5 cm/year is given in the lithosphere which is well within the limit of slow-spreading ridge (Table 5.1). The vertical velocity on the side boundaries of the lithosphere is zero. This mass outflux through the lithosphere is counter balanced by mass influx in the mantle in order to conserve total mass.

	Upper crust	Lower crust	Lithospheric mantle	Upper mantle	Plume	Seed	Sticky air
Density (kg m-3)	2750	2900	3325	3300	3275	3325	1
Grain size (m)			1e-3				
Thermal expansivities			2e-5				
Heat capacities			750				
Prefactors for dl (MPa^{-n} s^{-1})	1.1e-28	1.0e-21	2.41e-16	5.5e-16	5.5e-16	1.1e-28	1e-19
Stress exponents for dl	4.0	3.0	3.5	3	3	4.0	1
Activation energies for dl (J mol^{-1})	223.e3	356.e3	540.e3	540.e3	540.e3	223.e3	0
Activation volumes for dl (J Pa^{-1})	0	0	0	14e-6	14e-6	0	0
Prefactors for df (MPa^{-n} s^{-1})	1.1e-11	1e-11	2.41e-11	5.41e-11	5.41e-11	1.1e-11	1.92e-11
Grain size exponents for df	0	0	2.5	2.5	2.5	0	0
Activation energies for df (J mol^{-1})	223.e3	356.e3	540.e3	540.e3	540.e3	223.e3	335e3
Activation volumes for df (J Pa^{-1})	0	0	0	14e-6	14e-6	0	4e-6

Table 5.2: The initial boundary conditions

5.3   Simulation Results

Numerical simulations were performed in ASPECT Finite element modelling software in order to understand the dynamic plume lithosphere interaction based on the following parameters like the viscosity of the plume material with respect to the ambient mantle, the distance of separation between the plume axis and extensional rift axis in the lithosphere, the velocity of extensional rifting in the lithosphere and the viscosity of the lithosphere. The results for variation of each of the parameters are discussed below.

5.3.1 Separation between plume axis and rift axis (δ)

The distance between the axis through which plume rises in upper mantle and the location of weak zone due to horizontal rifting in lithosphere is denoted by δ. The rift velocity is same for all cases ie. 0.5 cm/ year.

When δ = 250 Km, the plume material rises through upper mantle and hits the base of lithospheric mantle at 0.8 My from start of simulation (Fig 5.7). After impinging the lithosphere, the plume material spreads laterally in both directions uniformly and causes delamination in the mantle lithosphere. Initially high strain zones are formed directly above the plume axis in lithosphere. At 1.29 My, a second pulse of plume hits the lithosphere causes thinning of mantle lithosphere and development of a high strain zone slightly to the left of plume axis, in the direction of motion of the rifting plate above. The velocity lines indicate that the development of this weak zone forces the plume head to impinge further into the lithosphere, slightly off set from its initial axis of ascent.

When δ = 200 Km, the plume head hits the base of lithosphere at 0.9 My (Fig. 5.8). After impinging the lithosphere, plume material flows laterally in both the directions towards and away from the rift axis. Initial impingement of plume at the base forms high strain in the lithosphere directly above the plume axis. However due to lateral flow, high strain zones disappear at 1.2 My after simulation start as evident from the strain rate results. Velocity flow lines show horizontal flow of lithospheric material above the stagnated plume material. So the plume material cannot impinge further into the lithosphere.

When δ = 150 Km, on the onset of plume head hitting the lithospheric mantle at 0.9 My, (Fig. 5.9) asymmetric high strain zones develop in lithosphere towards the rifting axis. So when the plume impinges further into the lithosphere it moves towards the rift axis. Hence, plume material accumulates under the rift axis. In this model, the lateral flow happens more on the side opposite to rift axis, causing asymmetric delamination of lithospheric mantle.

5.3.2 Rifting velocity in lithosphere (Vp)

Velocity of rifting is the velocity with which the lithospheric plates move away from each other. Here simulations are performed at a separation δ = 200 Km at different Vp.

When Vp = 0.5cm/year, the plume head hits the base of lithosphere at 0.9 My (Fig. 5.10). After impinging the lithosphere, plume material flows laterally in both the directions towards and away from the rift axis. The lateral flow causes deamination in lithospheric mantle.

δ = 250 Km, Vp = 0.5cm/yr

0.4 My　　0.6 My　　1.6 My　　2.5 My　　3 My

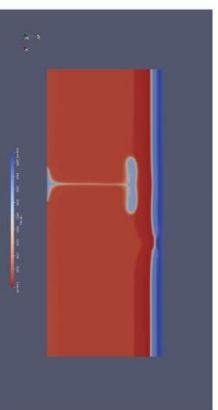Density　　　Strain Rate　　　Velocity
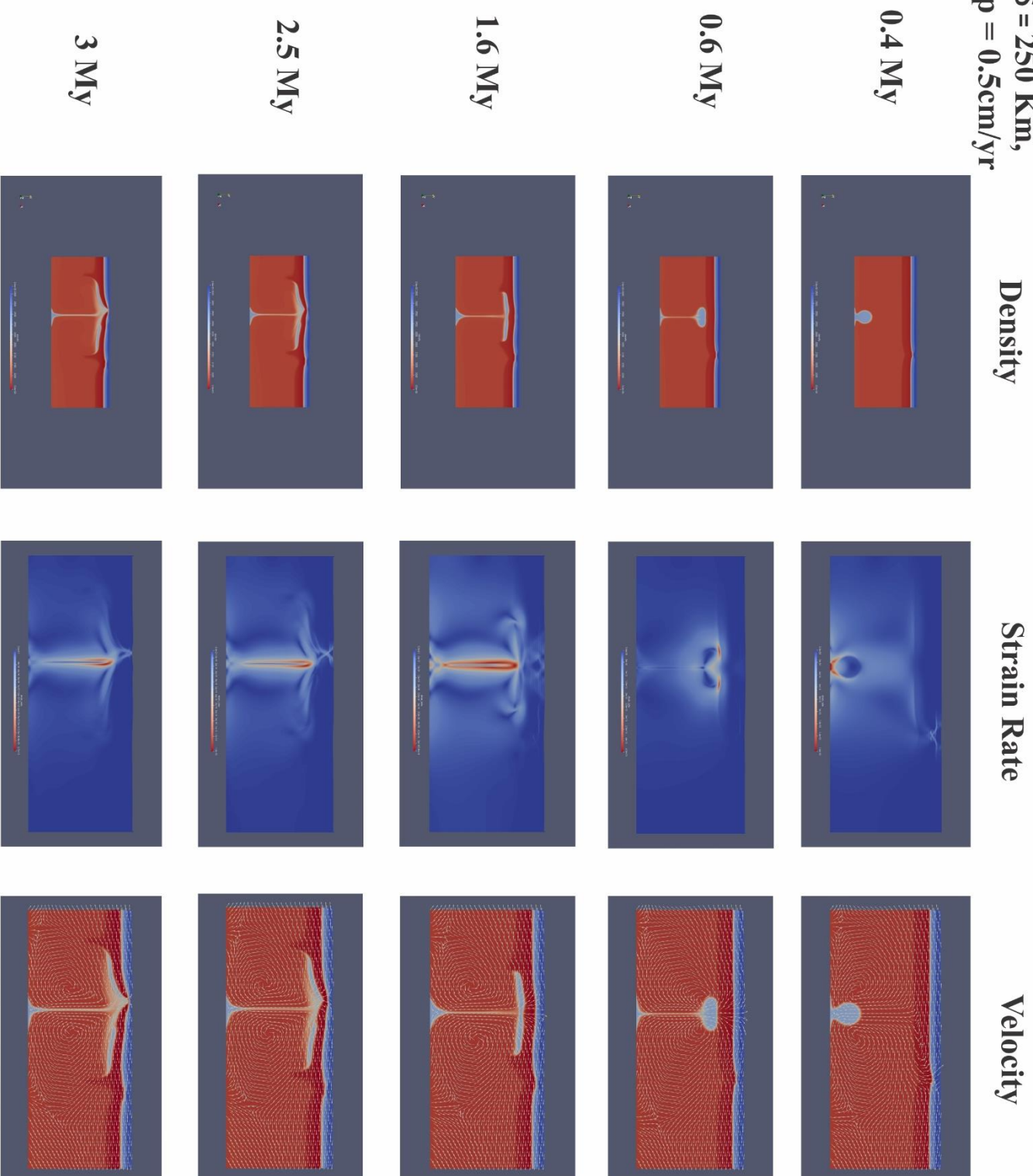
Fig. 5.7: Density, strain rate, flow velocity during evolution of low viscosity coupled plume respectively for δ = 250Km, Vp = 0.5 cm/year
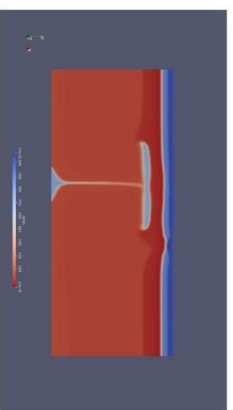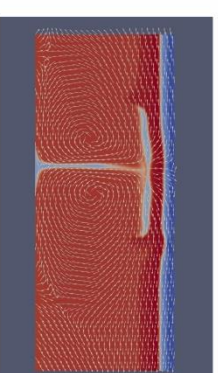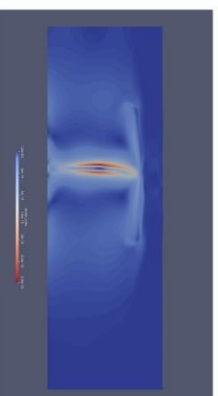
71

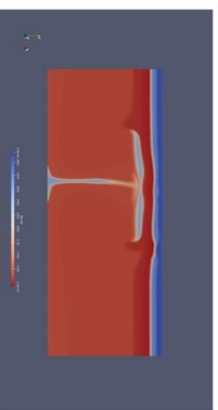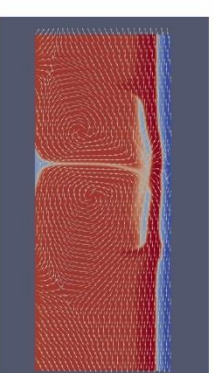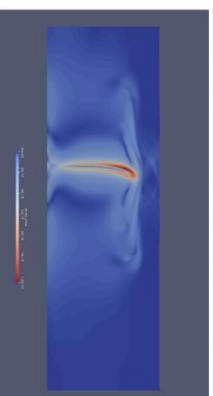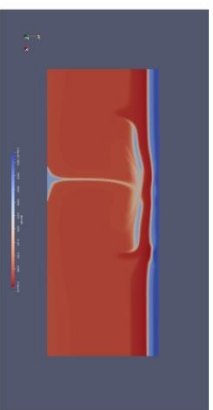**Density** **Strain Rate** **Velocity**

0.4 My
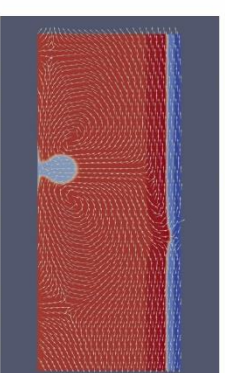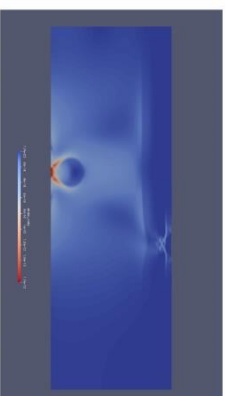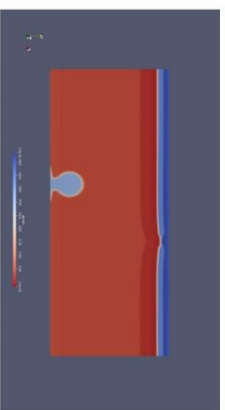
0.6 My
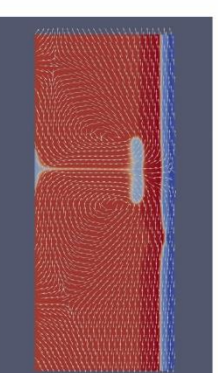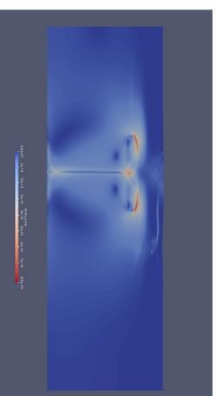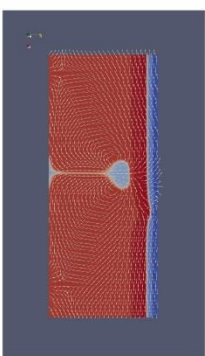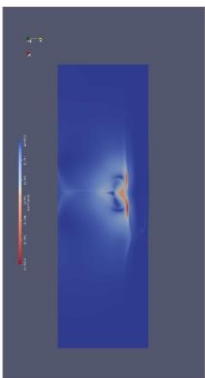
1.5 My
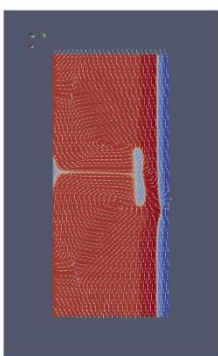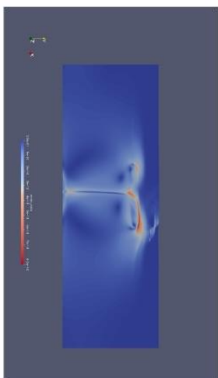
2.4 My

3 My

Fig. 5.8: Density, strain rate, flow velocity during evolution of low viscosity coupled plume respectively for δ = 200Km, Vp = 0.5 cm/year
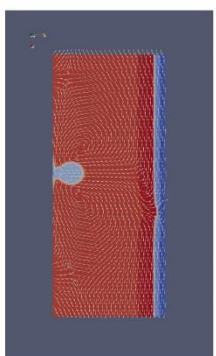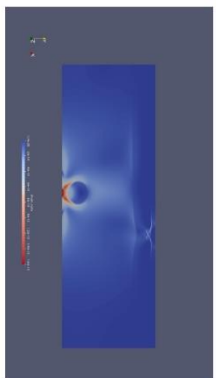
Fig 5.9: Density, strain rate, flow velocity during evolution of low viscosity coupled plume respectively for δ = 150Km, Vp = 0.5 cm/year.

δ = 150 Km, Vp = 0.5cm/yr
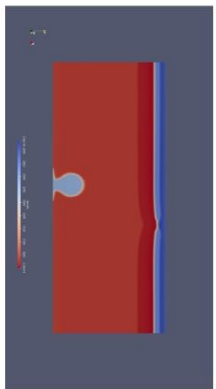
0.4 My

0.6 My

1.6 My

2.5 My

3 My

Density

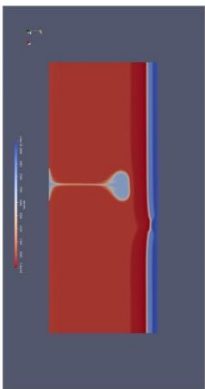Strain Rate

Velocity

When Vp = 1 cm/ year, the plume impinges the base of lithosphere at 0.8 My (Fig 5.10).After impinging it spreads laterally. When a second pulse of plume reaches the head, it causes weakening of the lithosphere and penetrates into the lithosphere slightly away from the plume axis, towards the motion of lithospheric plate.

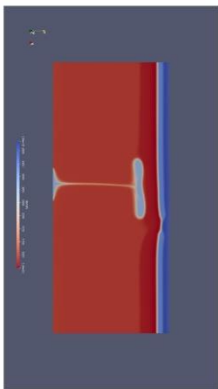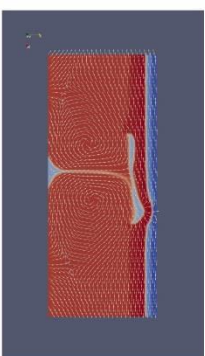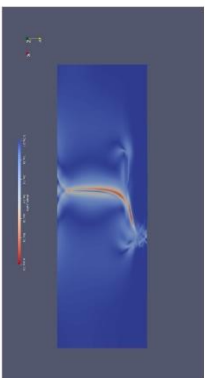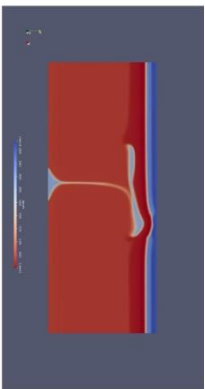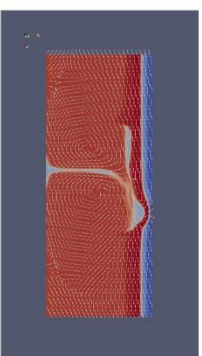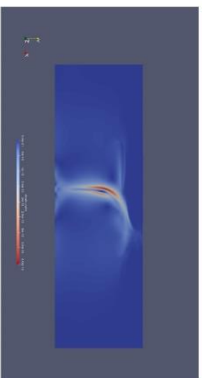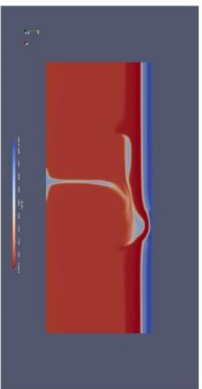When Vp = 5cm/year, the shape of the plume head is distorted due to mantle flow, even before hitting the lithospheric mantle boundary (Fig 5.10). The plume head has asymmetric shape with respect to the plume axis. The head is tilted more towards the direction of rift axis. After impinging the base, the plume head flows towards the rift channelized through the lithosphere.

5.3.3 Viscosity of Plume with respect to lithospheric mantle (η)

The model is based on the change in rheological contrast between the plume and lithosphere and how it changes the dynamics of plume lithosphere interaction when a weak zone of rifting is present directly above the plume axis.

When the η is low and has a coupled rheology with respect to lithospheric mantle, the plume morphology is mushroom shaped. The plume hits the base of the lithosphere at 10-15 My (Fig. 5.11). After the initial impingement, the head part penetrates through the lithosphere without much horizontal lateral flow. The strain rate shows initially when the plume rises, conjugate sets of high strain rate zone are formed in the lithosphere. However the influence of high strain zones due to rifting is reduced as the plume penetrates through the lithosphere (15-20 My). The temperature isotherms become constricted maximum at the point above plume head as the plume penetrates. Velocity diagrams show that the maximum velocity

3 My   **9 My**   **13 My**   **18 My**

Vp = 0.5 cm/year

3My   **4 My**   **9My**   **15My**

Vp = 1cm/year

.2My   **.4My**   **.5My**   **.6My**

Vp = 5cm/year
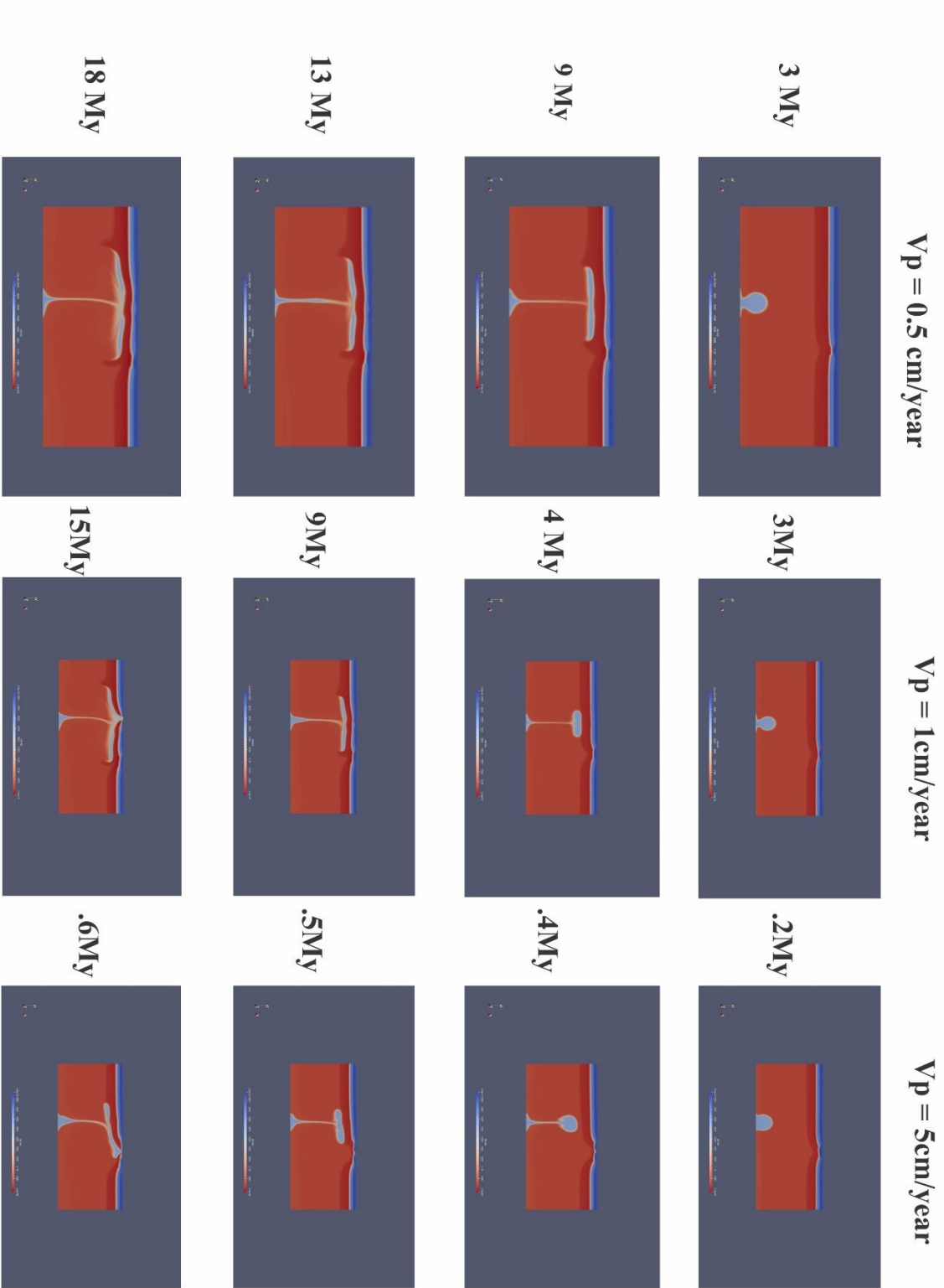
Fig 5.10: Density distribution during evolution of low viscosity coupled when δ = 200, for Vp = 0.5 cm/year, Vp = 1cm/year, Vp = 1.5 cm/year

75

Of the plume is in the central part where hot buoyant plume material rises through the stem.

When η is low ie. Plume material has a low viscosity with no coupling, simulation results show ascent of plumes with bulbous head and slender tail through lithospheric mantle. As the plume reaches the base of lithosphere at 25 My, the head flattens and new pulses of plume material accumulates (Fig 5.12). Due to the accumulation of buoyant material into the head, the flattened head rises through the lithosphere causing widespread lithospheric erosion. This causes widespread lithosphere thinning for about 50 Km on both sides of the rift axis. The high strain rate zone is distributed on either sides of the rift is weakened as the plume rises and high strain zones are limited to 30 Km on either side of rift axis. The velocity diagrams show that the high velocity stem reaches to a shallower level compared to the former model channelizing more buoyant material to shallower depth until 40 My.

When η is moderate with respect to mantle, the plume rises slowly. The shape of the ascending head is like a spout. As it reaches the base of the lithosphere at about 40 My (Fig 5.13). The plume material is not able to impinge into the crust, instead it flows laterally on either side of the plume axis. This causes most wide spread thinning of the lithosphere. Supply of buoyant material coupled with development of high strain rate zones ensures the rise to the plume material through lithosphere. The lithosphere thinning is affected to a distance of 100 Km on either side of rift axis. The velocity of flow in the central part is less compared to the previous models and the plume rises slowly penetrating and affecting larger areas in lithosphere.

Fig 5.11: Density, strain rate, temperature, and velocity during evolution of low viscosity coupled plume respectively. Here $\delta = 0$, Vp = 0.5 cm/year.

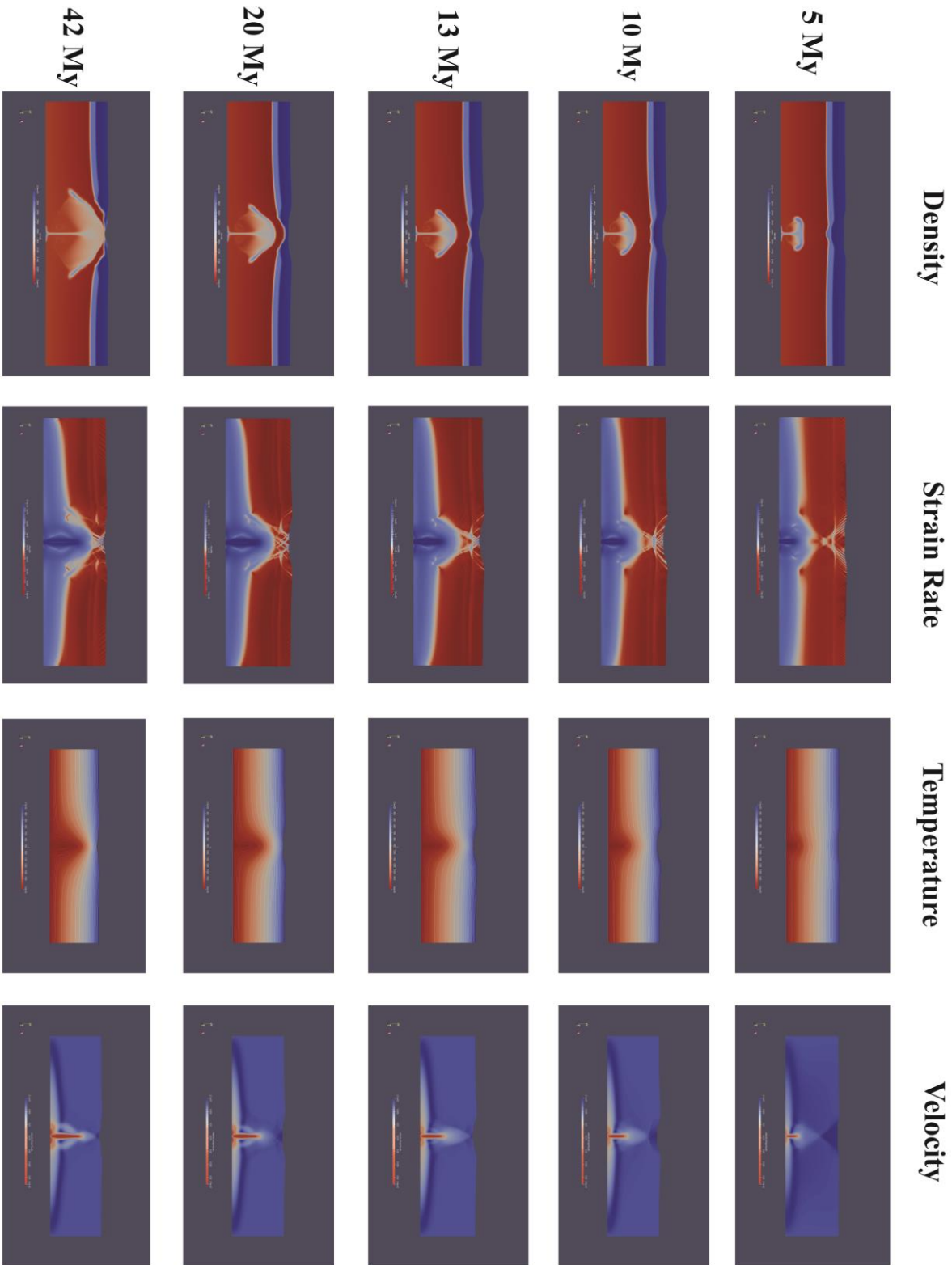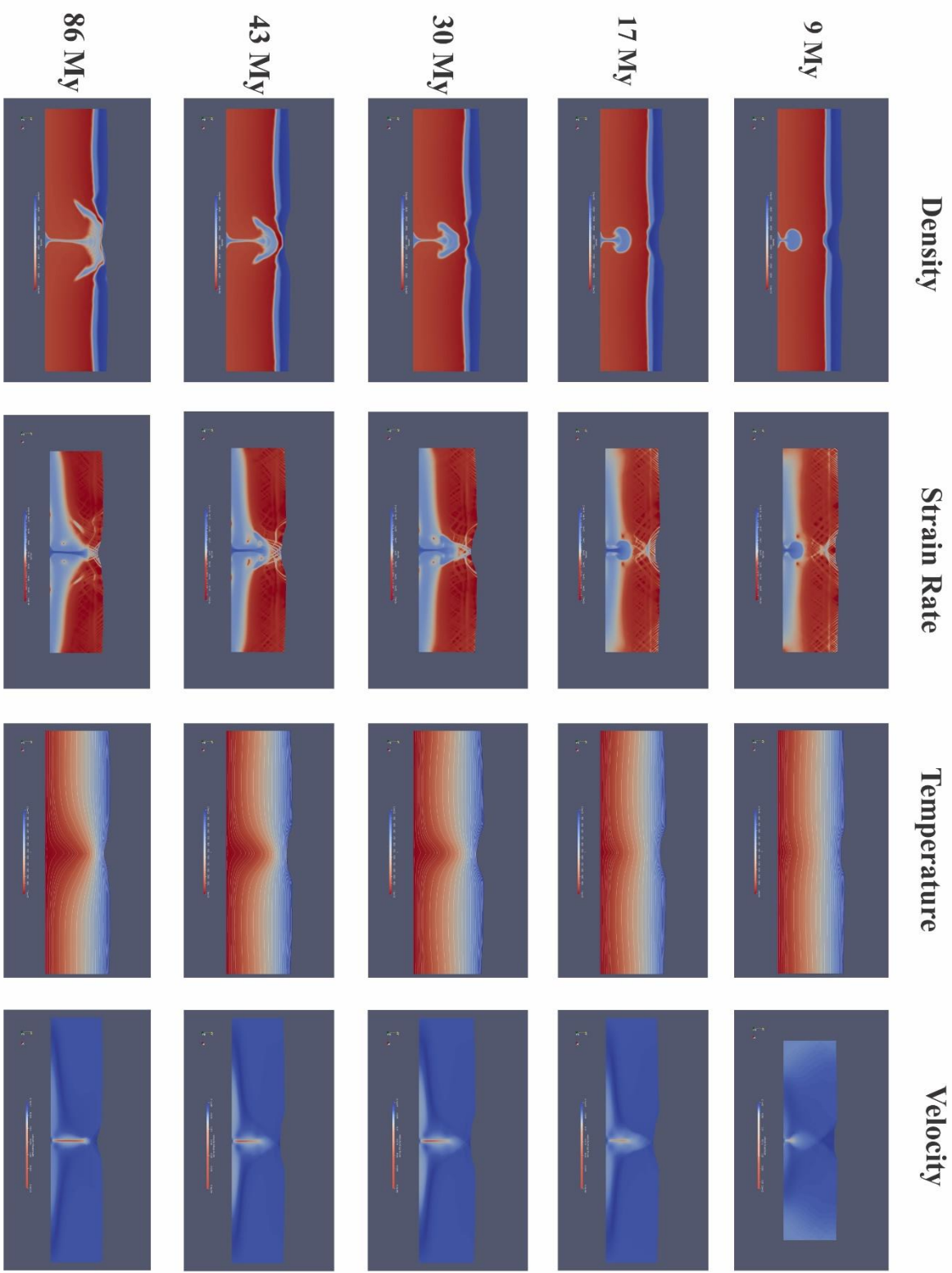Fig 5.12: Density, strain rate, temperature, velocity during evolution of low viscosity plumes. Here δ = 0, Vp = 0.5 cm/year.

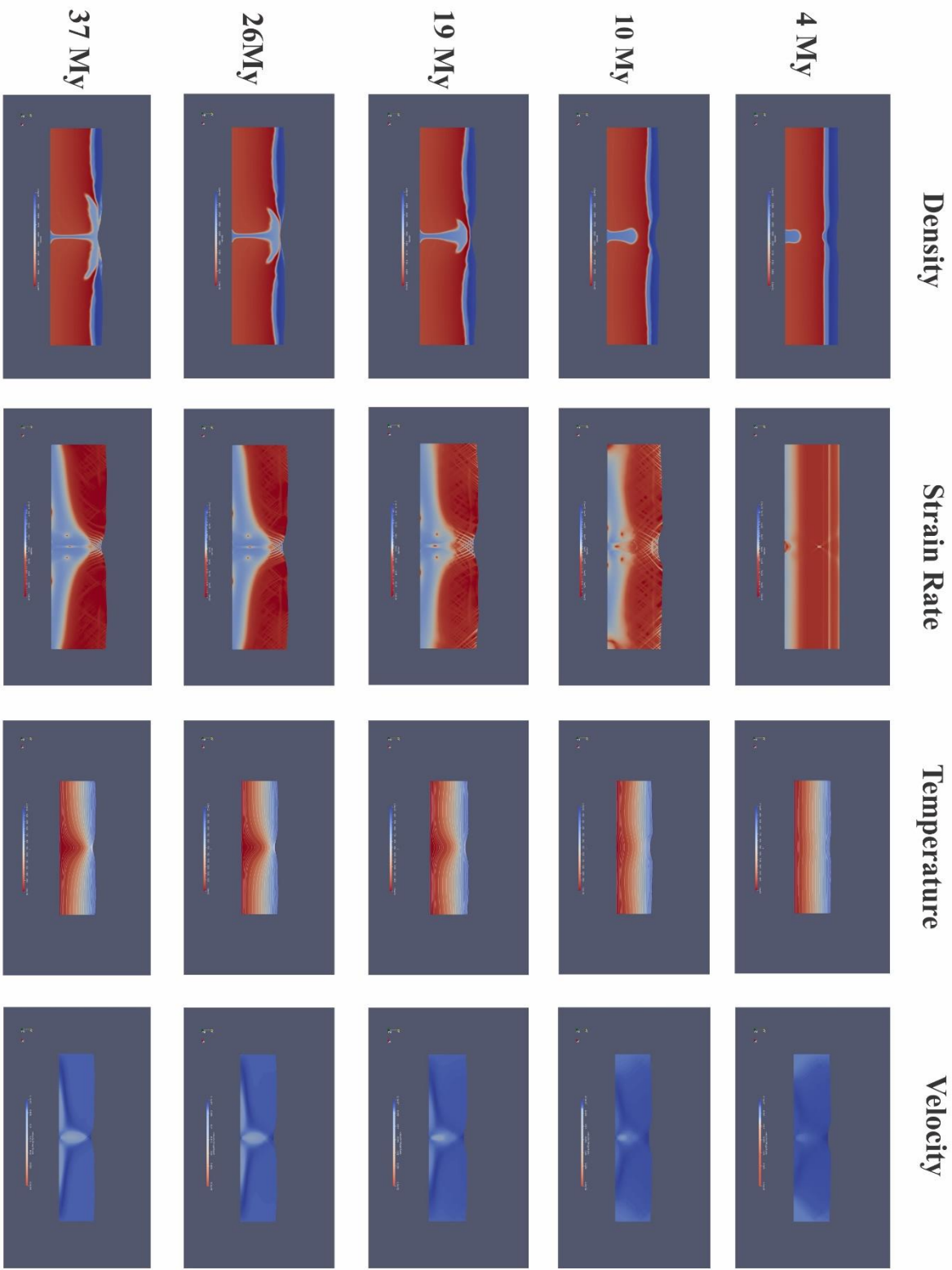Fig 5.13: Density, strain rate, temperature, velocity during evolution of moderate viscosity plumes. Here δ = 0, Vp = 0.5 cm/year.

Density   **Strain Rate**   **Temperature**   **Velocity**

37 My   26My   19 My   10 My   4 My

5.3.4 Viscosity of the lithosphere

In this simulation experiment, the lithosphere viscosity is changed to understand the response of plume interaction. Plume viscosity is low with respect to mantle and rift axis plume axis coincide with each other. The rift rate is 0.5 cm /year.

When viscosity of the lithosphere in low, the plumes penetrates directly into the lithospheric mantle. As the plume rises, widespread delamination causes thinning of lithosphere for about 150 Km on each side of the rifting. The plume material rises quickly though the lithosphere as it penetrates (Fig. 5.14)

When viscosity of lithosphere is high, the delamination is less compared to the previous model. The boundary between high viscosity lithosphere and mantle bends as the head reaches the base of the lithosphere at 0.8 My (Fig 5.14) The central portion of plume head penetrates into the lithosphere, while the peripheral portions flow laterally.

5.3.5 Maximum and Minimum topography

Maximum and minimum topography is measured in the model where different viscosity of plume material is used. Due to active rifting, the lithosphere undergoes extension. Since the lithosphere is intercalated with brittle and ductile layers, rifting causes topography to increase in parts of lithosphere and decrease like that in boudinage. With progressive extension, the maximum and minimum topography thus increases and decreases in lithosphere. However, when the plumes of

High viscosity lithosphere   Low Viscosity lithosphere

0.4 My   0.1 My

0.6 My   0.3 My

0.8 My   0.5 My

1.3 My   1 My
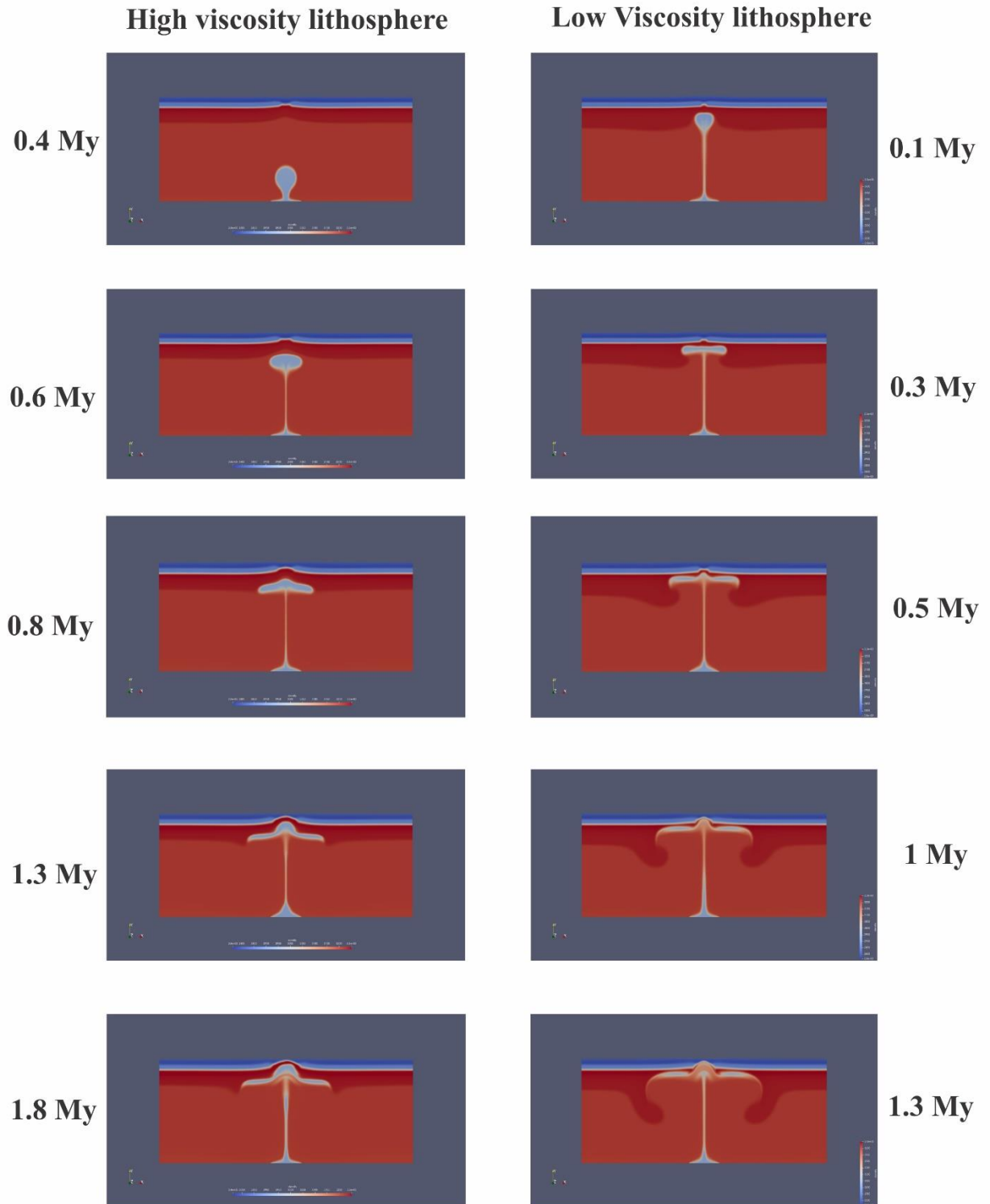
1.8 My   1.3 My

Fig 5.14: Results for high and low viscosity lithosphere for co axial rift and plume axis, vp = 0.5 cm/year, considering low viscous plume rheology

different viscosity (η) impinges the base of actively rifting lithosphere, the topographic response becomes different. When η is low with coupled mantle, the maximum topography steeply rises to a height of 2700 m at 10 My. (Fig. 5.15) But the rise of maximum topography is constrained by the plume after 10 My. The maximum topography thus decreases with time and again ceases to rise after 30 My. So the plume material prevents the rise of maximum topography in active rifting. In case of η being low without coupled mantle, the maximum topography also rises steeply but at a lower rate than the former situation. The maximum topography reaches 3400 m after 25 My (Fig. 5.15). After that it gradually falls and then again starts to rise after 36 My like previously. But when the viscosity η is moderate, plume rises slowly cannot prevent the rise of maximum topography. The maximum topography shows a positive slope, where it reaches a height of 8000 m after 15 My (Fig 5.15). In case of minimum topography, it reaches a shows a decreasing trend initially, then it rises to a peak after which it starts to fall again for both low viscosity coupled and non-coupled plumes. The lowest point is reaches at the same point of time when topography reaches maximum for both the cases. It then shows an increasing trend reaching a peak of at 14 My and 34 My respectively (Fig. 5.15). In both the cases they rise to about 2000m from the lowest point in minimum topography. After the respective peaks, the topography begins to fall. The response is different when η is high, the minimum topography falls to the lowest point of 6000 m below the substratum at 60 My (Fig. 5.15). After that it begins to rise and does not show a decreasing trend with time unlike the other two situations.
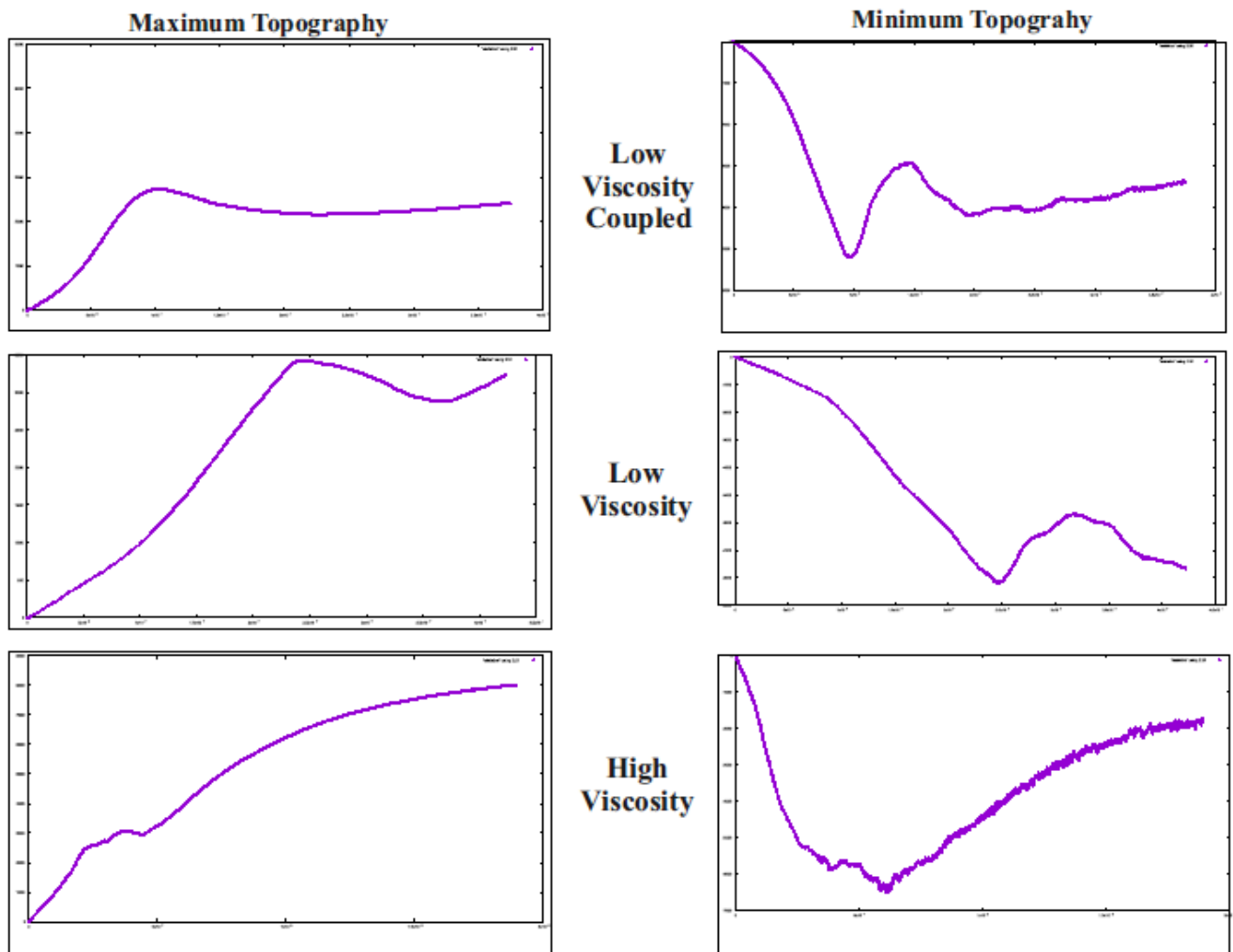
Fig 5.15: Maximum and minimum topography for co axial rift and plume axis, vp = 0.5 cm/year, considering low viscous plume rheology

Chapter 6

Discussion and Conclusion

The plume lithosphere interaction is a dynamic process. The interaction results in geologic features like dynamic topography over hotspots, plume under plating, erosion of sub lithospheric mantle. Subsequently it also results in generation of huge amount of melts in Ocean Island Basalts and Large Igneous Provinces, followed by a phase of eruption activity in OIBs forming chains of age progressive volcanic island. Classical literature reviews show that the plume morphology is affected by the physical parameters of the mantle and plume material. Review of plume-lithosphere interactions literature point out that the topography and lateral flow of plume material is controlled by the viscosity and density contrast between plume and lithosphere. The nature of topography is also influenced by the rheological layering in the crust. Velocity of lithospheric plates and the morphology of lithosphere plate control the rate and nature of plume under plating. In this thesis, physical experiments are performed by varying the viscosity contrast of plume-mantle to understand the changing interactions. For the lithosphere we use

a high viscosity layer of PDMS. The results show with increasing viscosity contrast, the dynamics of plume changes from continuous volume flux to pulsating volume flux. The interactions show that in the former case, maximum volume of plume material stagnates at the point of plume-lithosphere impact. While the latter study show pulses of high volume material accumulating successively along a trail as the plate moves. A sharp surface topography in lithosphere is observed during the study. However the topography cannot be measured quantitatively due to lack of apparatus that can measure the topography with high precision. Numerical simulation using ASPECT are performed to understand the plume lithosphere interaction in an active rift setting. Distance of separation between plume axis and rift axis, velocity of rifting are the main controlling factors that determine whether the plume material will flow towards the rift or not. The probability of plume flowing towards rift increases for a separation less than 150 Km and a rift velocity higher than 5 cm/year. Varying the viscosity contrast of plume-lithospheric mantle show change in morphology during plume ascent as well as difference in the under plating and lithospheric delamination. Viscosity contrast also changes the response of maximum and minimum topography. The lithosphere viscosity is also crucial parameter to understand the lithosphere erosion. Low lithosphere viscosity show extensive delamination of lithospheric mantle compared to high viscosity lithosphere.

References

Albers M, Christensen UR (1996) The excess temperature of plumes rising from the core-mantle boundary. Geophys Res Lett 23:3567–3570

Bercovici D, Mahoney J (1994) Double flood basalts and plume-head separation at the 660 km discontinuity. Science 266:1367–1369

Campbell IH, Griffiths RW (1990) Implications of mantle plume structure for the evolution of flood basalts. Earth Planet Sci Lett 99:79–93

Christensen U (1984) Instability in a hot boundary layer and initiation of thermochemical plumes. Ann Geophys 2:311–320

Christensen U (1985) Heat transport by variable viscosity convection II: Pressure influence, non-Newtonian rheology and decaying heat sources. Phys Earth Planet Int 37:183–205

Christensen UR, Harder H (1991) 3-D Convection with variable viscosity, Geophys J Int 104:213–226

Christensen UR, Hofmann AW (1994) Segregation of subducted oceanic crust in the convecting mantle, J. Geophys. Res 99:19867–19884

Condie KC (2001) Mantle plumes and their record in Earth history, Cambridge University Press, Cambridge

Coulliette DL, Loper DE (1995) Experimental, numerical and analytical models of mantle starting plumes. Phys Earth Planet Int 92:143–167

Davaille A, Jaupart C (1993) Transient high-Rayleigh number thermal convection with large viscosity variations, J. Fluid Mech 253:141–166

Davaille A (1999a) Two-layer thermal convection in miscible viscous fluids. J Fluid Mech 379:223–253

Davaille A (1999b) Simultaneous generation of hotspots and superswells by convection in a heterogeneous planetary mantle. Nature 402:756–760

Davaille A, Girard F, Le Bars M (2002) How to anchor plumes in a convecting mantle?, Earth Planet Sci Lett 203:62–634

Davaille A, Le Bars M, Carbonne C (2003) Thermal convection in a heterogeneous mantle, C R Acad Sci G´eosciences, 335/1:141–156

Farnetani CG, Richards MA (1994) Numerical investigations of the mantle plume initiation model for flood basalt events. J Geophys Res 99:13813–13833

Farnetani CG, Richards MA (1995) Thermal entrainment and melting in mantle plumes. Earth Planet Sci Lett 136:251–267

Feighner MA, Richards MA (1995) The fluid dynamics of plume-ridge and plumeplate interactions: An experimental investigation. Earth Planet Sci Lett 129:171–182

Griffiths RW, Campbell IH (1990) Stirring and structure in mantle starting plumes. Earth Planet Sci Lett 99:66–78

Griffiths RW, Campbell IH (1991) Interaction of mante plume heads with the Earth's surface and the onset of small-scale convection. J Geophys Res 96:18295–18310 Ito G, Lin J, Gable CW (1996) Dynamics of mantle flow and melting at a ridgecentered hotspot: Iceland and the Mid-Atlantic Ridge. Earth Planet Sci Lett 144:53–74

Ito G, Lin J, Gable CW (1997) Interaction of mantle plumes and migrating midoceanic ridges: Implications for the Galapagos plume-ridge system. J Geophys Res 102:15403–15417

Ito G, Shen Y, Hirth G, Wolfe CJ (1999) Mantle flow, melting, and dehydration of the Iceland mantle plume. Earth Planet Sci Lett 165:81–96

Ito G (2001) Reykjanes 'V'-shaped ridges originating from a pulsing and dehydrating mantle plume. Nature 411:681–684

Ito G, Lin J, Graham D (2003) Observational and theoretical studies of the dynamics of mantle plume-mid-ocean ridge interaction. Rev Geophys 41: doi:10.1029/2002RG000117

Jellinek AM, Manga M (2002) The influence of a chemical boundary layer on the fixity, spacing and lifetime of mantle plumes. Nature 41:760–763

Montelli R, Nolet G, Dahlen FA, Masters G, Engdahl ER, Hung SH (2004) Finitefrequency tomography reveals a variety of plumes in the mantle. Science 303:338–

343 Olson P (1984) An experimental approach to thermal convection in a two-layered mantle. J Geophys Res 89:11293–11301

Olson P (1990) Hot spots, swells and mantle plumes. In: Ryan MP (ed) Magma transport and storage. John Wiley and Sons, New York, pp 33–51

Olson P, Singer H (1985) Creeping plumes. J Fluid Mech 158:511–531

Olson P, Nam IS (1986) Formation of seafloor swells by mantle plumes. J Geophys Res 91:7181–7191

Ribe NM, Christensen U (1994) Three-dimensional modeling of plume-lithosphere interaction. J Geophys Res 99:669–682

Richards MA, Griffiths RW (1988) Deflection of plumes by mantle shear flow: experimental results and a simple theory. Geophys J 94:367–376

Schubert G, Turcotte DL, Olson P (2001) Mantle convection in the Earth and planets, Cambridge University Press, Cambridge

Sleep NH (1996) Lateral flow of hot plume material ponded at sublithospheric depths. J Geophys Res 101:28065–2808

Van Keken P (1997) Evolution of starting mantle plumes: a comparison between numerical and laboratory models. Earth Planet Sci Lett 148:1–11

Whitehead JA, Luther DS (1975) Dynamics of laboratory diapir and plume models, J Geophys Res 80:705–717

Zhao D (2001) Seismic structure and origin of hotspots and mantle plumes. Earth Planet Sci Lett 192:251–265